

LRRK2 Is Recruited to Phagosomes and Co-recruits RAB8 and RAB10 in Human Pluripotent Stem Cell-Derived Macrophages

Heyne Lee,¹ Rowan Flynn,¹ Ishta Sharma,¹ Emma Haberman,¹ Phillippa J. Carling,^{2,3} Francesca J. Nicholls,⁴ Monika Stegmann,¹ Jane Vowles,^{1,2} Walther Haenseler,¹ Richard Wade-Martins,^{2,3} William S. James,¹ and Sally A. Cowley^{1,2,*}

¹Sir William Dunn School of Pathology, University of Oxford, South Parks Road, Oxford OX1 3RE, UK

²Oxford Parkinson's Disease Centre, University of Oxford, South Parks Road, Oxford OX1 3QX, UK

³Department of Physiology, Anatomy and Genetics, University of Oxford, South Parks Road, Oxford OX1 3QX, UK

⁴Department of Psychiatry, University of Oxford, Warneford Hospital, Oxford OX3 7JX, UK

*Correspondence: sally.cowley@path.ox.ac.uk

<https://doi.org/10.1016/j.stemcr.2020.04.001>

SUMMARY

The Parkinson's disease-associated gene, *LRRK2*, is also associated with immune disorders and infectious disease and is expressed in immune subsets. Here, we characterize a platform for interrogating the expression and function of endogenous *LRRK2* in authentic human phagocytes using human induced pluripotent stem cell-derived macrophages and microglia. Endogenous *LRRK2* is expressed and upregulated by interferon- γ in these cells, including a 187-kDa cleavage product. Using *LRRK2* knockout and G2019S isogenic repair lines, we find that *LRRK2* is not involved in initial phagocytic uptake of bioparticles but is recruited to LAMP1⁺/RAB9⁺ “maturing” phagosomes, and *LRRK2* kinase inhibition enhances its residency at the phagosome. Importantly, *LRRK2* is required for RAB8a and RAB10 recruitment to phagosomes, implying that *LRRK2* operates at the intersection between phagosome maturation and recycling pathways in these professional phagocytes.

INTRODUCTION

LRRK2 (leucine-rich repeat kinase 2) encodes a large (286 kDa), multi-domain cytoplasmic protein, with both guanosine triphosphatase (GTPase) and kinase domains, flanked by several protein-protein interaction domains. Mutations in *LRRK2* account for approximately 4% of familial and 1% of idiopathic cases of the progressive neurodegenerative disorder, Parkinson's disease (PD), forming an important genetic risk factor for PD. Most PD-causing mutations cluster within the two enzymatic sites, notably G2019S and R1441C/G (leading to a modest 2- to 3-fold increase in kinase activity and decreased GTPase activity, respectively) (Ferreira and Massano, 2017). *LRRK2* variants are also associated with autoimmune disorders (Witoelar et al., 2017), particularly Crohn's disease, and with infectious diseases, notably *Mycobacterium leprae* (Wang et al., 2015; Zhang et al., 2009). *LRRK2* expression has also been linked with *Mycobacterium tuberculosis* infection (Härtlova et al., 2018; Wang et al., 2018). *LRRK2* is expressed in a variety of cell lineages, including several immune subsets, notably B cells, neutrophils, monocytes, macrophages, and microglia (Atashrazm et al., 2019; Fan et al., 2018; Gardet et al., 2010; Hakimi et al., 2011; Kim et al., 2012; Marker et al., 2012; Moehle et al., 2012; Thévenet et al., 2011; reviewed in Lee et al., 2017).

Macrophages populate most tissues of the body, deriving initially from primitive macrophages that migrate in during embryogenesis, and are replenished as necessary during the lifespan by either local proliferation and/or replacement by blood monocyte-derived macrophages, depend-

ing on the tissue (Hoeffel and Ginhoux, 2015). Macrophages perform tissue homeostatic functions and are also a first-line defense against pathogens, armed with a plethora of pattern-recognition and opsonin receptors. They rapidly phagocytose and kill incoming bacteria, fungi, and protozoists, and have strong antiviral defenses. Nonetheless, various pathogens can overcome these defenses to survive and proliferate in macrophages, including *M. leprae* and *M. tuberculosis*. Interestingly, *LRRK2* has recently been shown to be required for survival of *M. tuberculosis* in macrophages (Härtlova et al., 2018).

Microglia are a resident, primitive macrophage-derived population in the central nervous system, performing homeostatic functions (phagocytosing cell debris, extracellular protein aggregates, and incompetent synapses) to maintain a healthy environment for neurons. However, they can also secrete inflammatory mediators when activated, notably tumor necrosis factor α , and a myriad of cytotoxic factors, especially reactive oxygen species and nitric oxide, which can instigate a feedforward cycle of chronic inflammation and neurodegeneration. Therefore, microglia are not only involved in preventing neurodegenerative disease by phagocytosing potentially harmful materials but also can contribute to disease progression by initiating exaggerated inflammatory responses (reviewed in Wolf et al., 2017).

Due to the difficulty in obtaining primary patient material, most studies of *LRRK2* have used animal models, *in vitro* biochemical assays, or transformed cell lines, often involving non-physiological exogenous overexpression of *LRRK2* in irrelevant lineages. Studies of *LRRK2* using



A KO of *LRRK2*

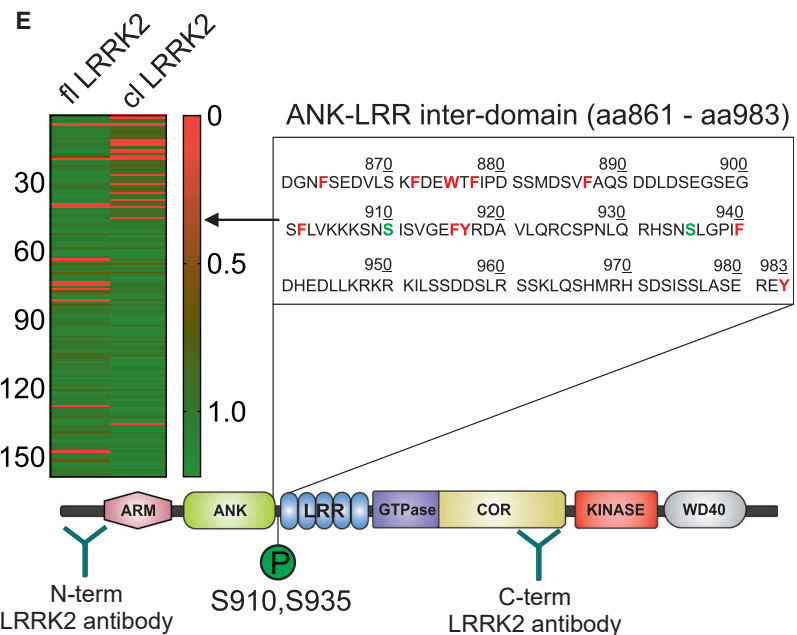
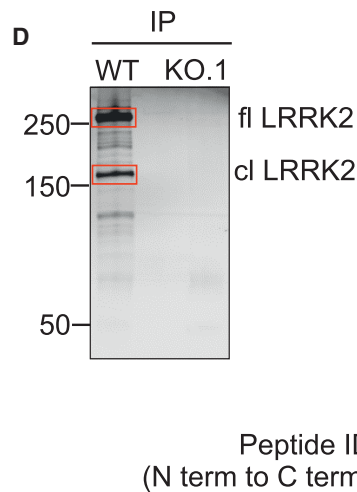
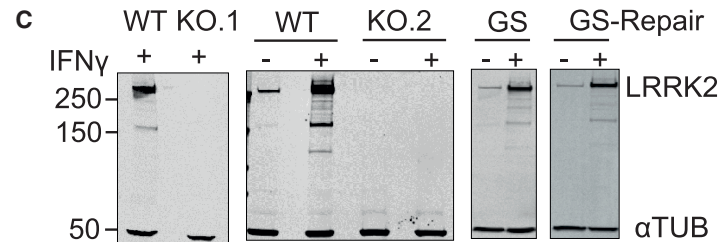
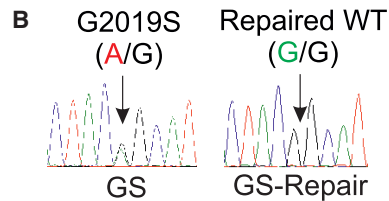
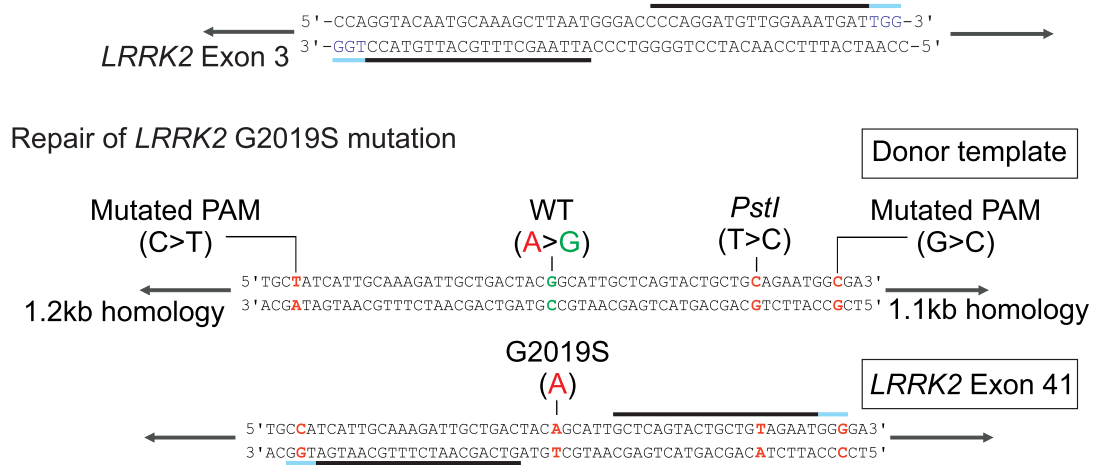


Figure 1. Characterization of *LRRK2* Knockout and G2019S Isogenic Control hiPSC Lines and a Major *LRRK2* Cleavage Product in Macrophages

(A) CRISPR/Cas-9-mediated knockout (KO) of *LRRK2* was performed using a double nickase strategy with a pair of guide RNAs (gRNAs, black lines; protospacer adjacent motif [PAM], blue lines) targeting exon 3 of *LRRK2*. For CRISPR/Cas-9-mediated repair of *LRRK2* G2019S mutation, the donor template contained silent mutations in the PAM site to maximize gene-editing efficiency and a *PstI* site for the subsequent screening of edited clones.

(legend continued on next page)



transformed myeloid cell lines have progressed this field (Gardet et al., 2010; Marker et al., 2012), and Eguchi et al. (2018) have reported that LRRK2 recruits and phosphorylates RABs 8 and 10 to chloroquine-induced overload-stressed lysosomes in mouse RAW264.7 cells, leading to release of lysosomal contents. Yet such observations need to be subsequently assessed in a karyotypically normal human cellular system at physiologically relevant expression levels to validate their applicability to normal human physiology and disease. We have previously developed methods for efficient differentiation of human induced pluripotent stem cells (hiPSCs) to macrophages, which exhibit authentic phagocytic properties and cytokine-profiles (Flynn et al., 2015; Haenseler et al., 2017b; Karlsson et al., 2008; van Wilgenburg et al., 2013). The differentiation pathway is demonstrably independent of c-Myb expression (Buchrieser et al., 2017), indicating that they represent an embryonic/primitive ontogeny and are therefore also suitable as a precursor for differentiation to microglia. We have shown that they can be further differentiated to microglia by co-culture with hiPSC neurons, whereupon they acquire a ramified morphology and associated neuronal surveillance activity (Haenseler et al., 2017a).

In this study, we have used hiPSC macrophages and microglia from patient, control, and gene-edited lines to explore the expression of LRRK2 protein from the endogenous locus and the role of LRRK2 in this lineage. We show that LRRK2 is expressed in hiPSC macrophages and microglia, with expression significantly upregulated by interferon- γ (IFN- γ) and identify the cleavage region of a truncated LRRK2 product found in this lineage. In this system, LRRK2 is not involved in the initial phagocytic uptake of particles but is recruited to maturing phagosomes, and this is exacerbated by inhibition of LRRK2 kinase activity. Importantly, we show that LRRK2 is required for recruitment to phagosomes of RAB8a and RAB10 (members of the membrane trafficking regulator family of RAB GTPases and substrates of LRRK2 kinase activity). This demonstrates that LRRK2 operates at the intersection between phagosome maturation and recycling pathways in the myeloid lineage.

RESULTS

Characterization of LRRK2 Knockout and G2019S Isogenic Control hiPSC Lines and a Major LRRK2 Cleavage Product in Macrophages

The hiPSC lines used in this study are listed in Table S1, with quality control information in Figure S1. Wild-type lines (WT.1 to WT.6) were from six healthy control donors.

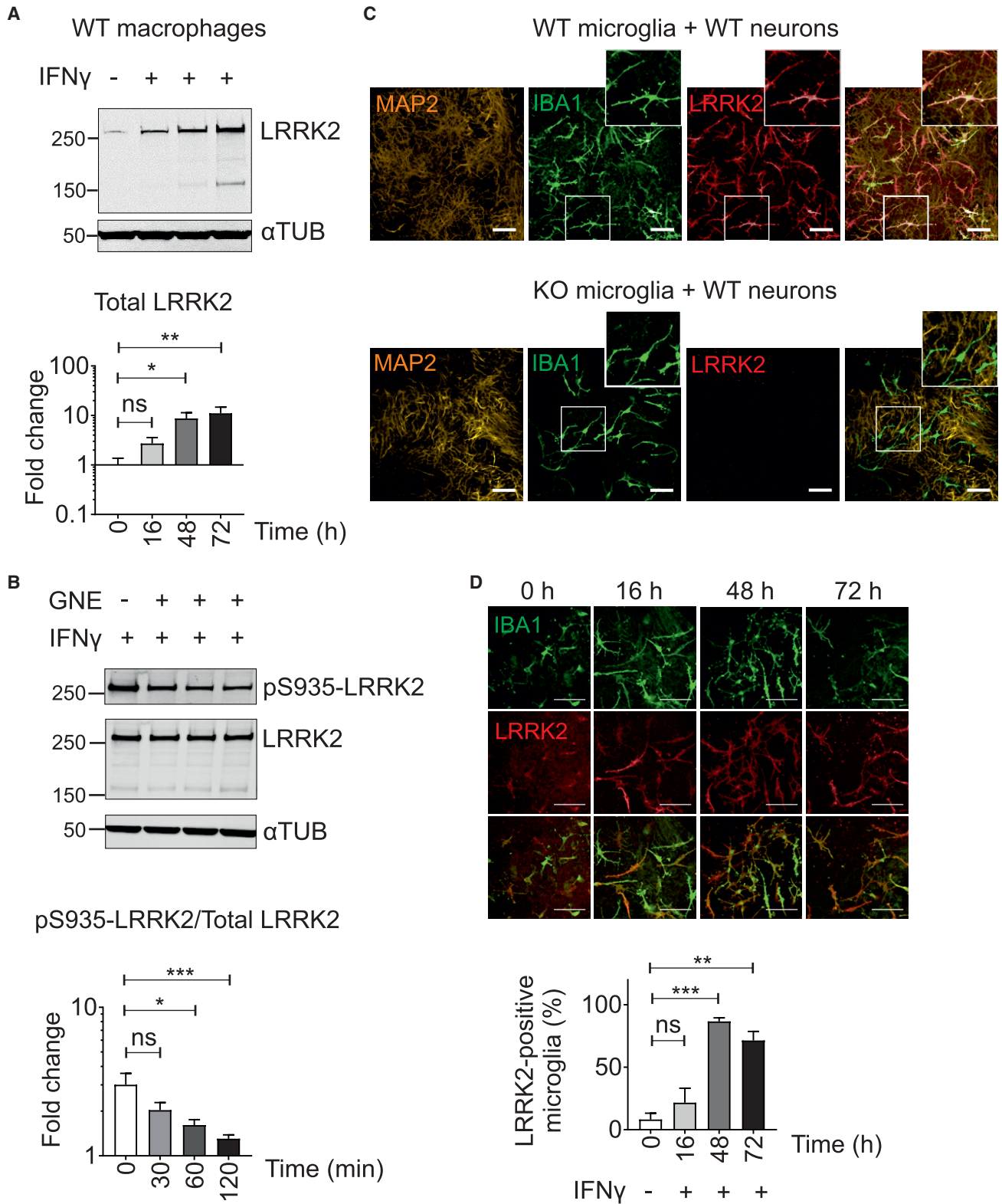
LRRK2 knockout (KO) was generated in a control hiPSC (line WT.1) by a double nickase CRISPR/Cas9 (Ran et al., 2013) strategy, using a pair of guide RNAs (gRNAs) targeting exon 3 of LRRK2 (Figures 1A and S2A). A patient line containing a heterozygous LRRK2 mutation G2019S (GS) was successfully repaired to WT (GS-Repair) as shown by sequence analysis (Figure 1B). Two KO clones (KO.1 and KO.2) displayed out-of-frame homozygous deletion of LRRK2 (Figure S1A) and showed complete absence of LRRK2 protein when differentiated to macrophages (Figure 1C). There was no significant difference in the production of macrophage precursors in edited versus parental lines (Figures S2B and S2C).

Western blot of hiPSC macrophages using LRRK2 monoclonal antibody N241A/34 (binding site amino acids [aa] 1,836–1,845) consistently showed multiple faint bands and a major band (approximately 170 kDa relative to size markers) in addition to full-length LRRK2 (286 kDa). This was particularly evident upon IFN- γ stimulation. The staining pattern was confirmed to be LRRK2 specific by its absence in LRRK2 KO hiPSC macrophages (Figure 1C). Since LRRK2 transcripts that would correspond to this product have not been reported, we reasoned that this is likely a proteolytically cleaved product. It is not a result of technical post-lysis proteolysis, as spiking recombinant full-length LRRK2 into LRRK2-KO macrophage lysate did not lead to its proteolytic degradation under our standard lysis conditions (Figure S2D). Addition of protease inhibitors to live macrophages reduced the proportion of the truncated versus full-length protein, implying that it is a natural cleavage generated within intact macrophages (Figure S2E). Immunoprecipitation using the N-terminal antibody revealed that the cleaved product can heterodimerize with

(B) Sequencing results demonstrate that the G2019S mutation present in one allele (A/G) was successfully corrected to the WT sequence (G/G). (C) Western blot probed with antibody to LRRK2 N241A/34 shows the complete absence of endogenous LRRK2 protein in both KO clones in hiPSC macrophages with or without 72-h IFN- γ (100 ng/mL) activation. The total expression level of LRRK2 protein in the isogenic repaired line is not altered. α TUB, α -tubulin.

(D) Western blot showing immunoprecipitated (N241A/34 antibody) endogenous LRRK2 protein from WT- and KO-derived hiPSC macrophages. Silver-stained gel bands corresponding to full-length LRRK2 (fl LRRK2) and the cleaved LRRK2 (cl LRRK2), indicated in red boxes, were cut and analyzed by mass spectrometry.

(E) Trypsin-digested peptides were quantified by MaxQuant. Heatmap shows the intensity of identified peptides (ordered from N terminus to C terminus) of fl LRRK2 and cl LRRK2. cl LRRK2 is largely missing N-terminal peptides up to ANK-LRR inter-domain aa 861–983 (chymotrypsin cleavage sites, red; phosphorylation sites, green).



(legend on next page)



full-length LRRK2 (Figures S2F and S2G). To identify the cleavage site, we isolated endogenous LRRK2 protein from hiPSC macrophages by immunoprecipitation with N241A/34 antibody, ran it on a denaturing gel, and analyzed the cleaved product by mass spectrometry (Figure 1D). Max-Quant analysis of trypsin-digested peptide fragments revealed that cleavage occurs within the ANK-LRR interdomain region (aa 861–983), generating a C-terminal predicted product of ~170–187 kDa (Figure 1E). Western blot of hiPSC macrophage whole-cell lysate using an antibody against LRRK2 pSer935, did not co-localize with the C-terminal cleavage product band but did co-localize with a ~110-kDa band detected by the N-terminal antibody, and treatment of the cells with LRRK2 kinase inhibitor GNE-7915 (GNE) reduced the intensity of the pSer935 band (Figure S2H). Together, these results indicate that S935 can be present on the N-terminal cleavage product, predicting the major cleavage site to be downstream of S935.

IFN- γ Increases LRRK2 Protein Expression in hiPSC Macrophages and Microglia

IFN- γ has been shown to upregulate LRRK2 protein expression in myeloid cells (Gardet et al., 2010). Similarly, in hiPSC macrophages, LRRK2 protein expression increased significantly (up to 10-fold) upon IFN- γ treatment (Figures 2A and S3A). Phosphorylation of LRRK2 at S935 was observed, significantly decreasing in the presence of LRRK2 kinase inhibitor GNE, in accordance with the published literature (Hatcher et al., 2017) (Figure 2B). hiPSC macrophages with the heterozygous G2019S mutation showed the same pattern, with no significant difference in either the basal phosphorylation level at S935 or the degree of dephosphorylation upon treatment with LRRK2 kinase inhibitors compared with its isogenic pair (Figure S3B), likely because G2019S only produces a modest 2-fold increase in kinase activity.

We next examined LRRK2 expression in hiPSC microglia, co-cultured with hiPSC cortical neurons. LRRK2 protein was clearly expressed in hiPSC microglia while its expres-

sion level was not detectable in hiPSC cortical neurons (Figure 2C). The specificity of LRRK2 staining in microglia was confirmed by co-culturing microglia differentiated from LRRK2 KO hiPSCs with cortical neurons differentiated from LRRK2 WT hiPSCs (Figure 2C). To test whether IFN- γ upregulates LRRK2 protein in hiPSC microglia or neurons, we treated hiPSC microglia/cortical neuron co-cultures with IFN- γ for 16 h, 48 h, or 72 h. IFN- γ treatment significantly upregulated the percentage of LRRK2 expressing hiPSC microglia to 86%, its expression level plateauing by 48 h post IFN- γ treatment (Figure 2D).

Together, these results demonstrate the validity of the hiPSC macrophage and microglia models for investigating endogenous LRRK2 function.

LRRK2 Is Not Involved in the Initial Phagocytic Uptake of Bioparticles but Is Recruited to Maturing Phagosomes

We next investigated whether LRRK2 is involved in phagocytosis using hiPSC macrophages. hiPSC macrophages readily phagocytose a wide variety of “meals,” including killed yeast bioparticles (“zymosan”), a process ablated by inhibiting actin polymerization with cytochalasin D. Complete absence of LRRK2 in hiPSC macrophages did not alter their ability to take up fluorescent zymosan, with or without IFN- γ induction (Figures 3A and 3B). Similarly, zymosan uptake by G2019S patient-derived hiPSC macrophages was not significantly different from that of its isogenic pair (Figure 3C). Lastly, pharmacological inhibition of LRRK2 kinase activity with two structurally distinct LRRK2 kinase inhibitors, GSK2578215A (GSK) or GNE, had no significant effect on zymosan uptake (Figure 3D). Acidification of the phagosomes, as assessed by uptake of pH-sensitive fluorescent (pHrodo) zymosan particles, was also not significantly altered by manipulating LRRK2 in hiPSC macrophages (Figure S4).

While no functional difference in initial phagocytic uptake was observed across LRRK2 lines, confocal imaging

Figure 2. IFN- γ Increases LRRK2 Protein Expression in hiPSC Macrophages and Microglia

(A) hiPSC macrophages were treated with IFN- γ (100 ng/mL) for 16, 48, and 72 h and cell lysates were analyzed by western blot. Bar graph shows fold change of the total endogenous LRRK2 protein over loading control (α -tubulin [α TUB]). (B) hiPSC macrophages were treated with LRRK2 kinase inhibitor GNE-7915 (GNE; 1 μ M) for 30, 60, and 120 min after 72-h treatment with IFN- γ . Bar graph shows fold change in pS935-LRRK2 signal over total LRRK2 relative to DMSO control. All data points in (A) and (B) represent mean \pm SEM of at least three independent experiments. (C) Microglia differentiated from either WT or KO hiPSC were co-cultured with cortical neurons differentiated from WT hiPSC. Cells were treated with IFN- γ (100 ng/mL) for 48 h and were stained with antibodies against neuronal marker (MAP2), microglial marker (IBA1), and LRRK2 (N241A/34). (C) and (D) scale bars represent 100 μ m. (D) hiPSC microglia co-cultured in hiPSC neurons were treated with IFN- γ (100 ng/mL) for 0, 16, 48, and 72 h. z-stacked confocal images were acquired and the number of hiPSC microglia (IBA1-positive cells) expressing LRRK2 was quantified using Columbus software (PerkinElmer). Bar graph shows percentage of LRRK2-expressing hiPSC microglia as mean \pm SEM of three independent experiments. (A), (B) and (D) statistical significance was tested using one-way ANOVA, * p < 0.05, ** p < 0.01, *** p < 0.001, not significant, ns: p > 0.05. Generation of LRRK2 modified hiPSC lines.

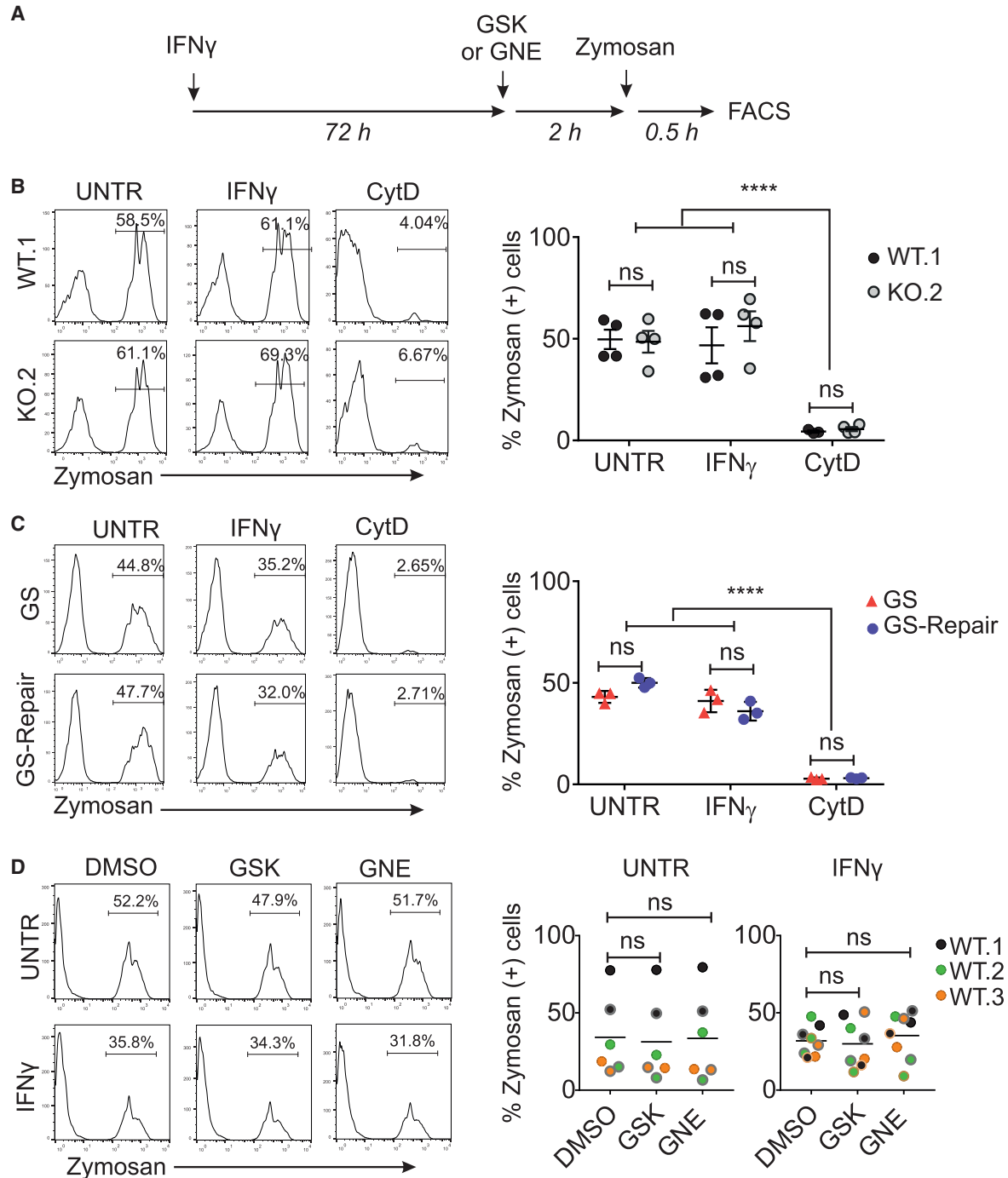


Figure 3. LRRK2 Is Not Involved in the Initial Phagocytic Uptake of Bioparticles

(A) Outline of the experimental design.

(B and C) hiPSC macrophages differentiated from the two isogenic pairs (B, WT and KO; C, GS and GS-Repair) were treated with IFN- γ for 3 days, then pre-treated with either DMSO or 10 μ M cytochalasin D (CytD, to inhibit actin polymerization as a negative control) for 1 h before incubation with Alexa Fluor 488-conjugated zymosan bioparticles for 30 min. Bar graphs show the percentage of zymosan⁺ cells as mean \pm SEM.

(D) hiPSC macrophages from three healthy controls (WT.1, WT.2, WT.3) were pre-treated with LRRK2 kinase inhibitors (GNE or GSK; 1 μ M) prior to the addition of zymosan bioparticles. Each dot represents data from each independent experiment. (B-D) two-way ANOVA with Dunnett multiple comparisons was used for statistical analysis, ****p < 0.0001, not significant, ns: p > 0.05.

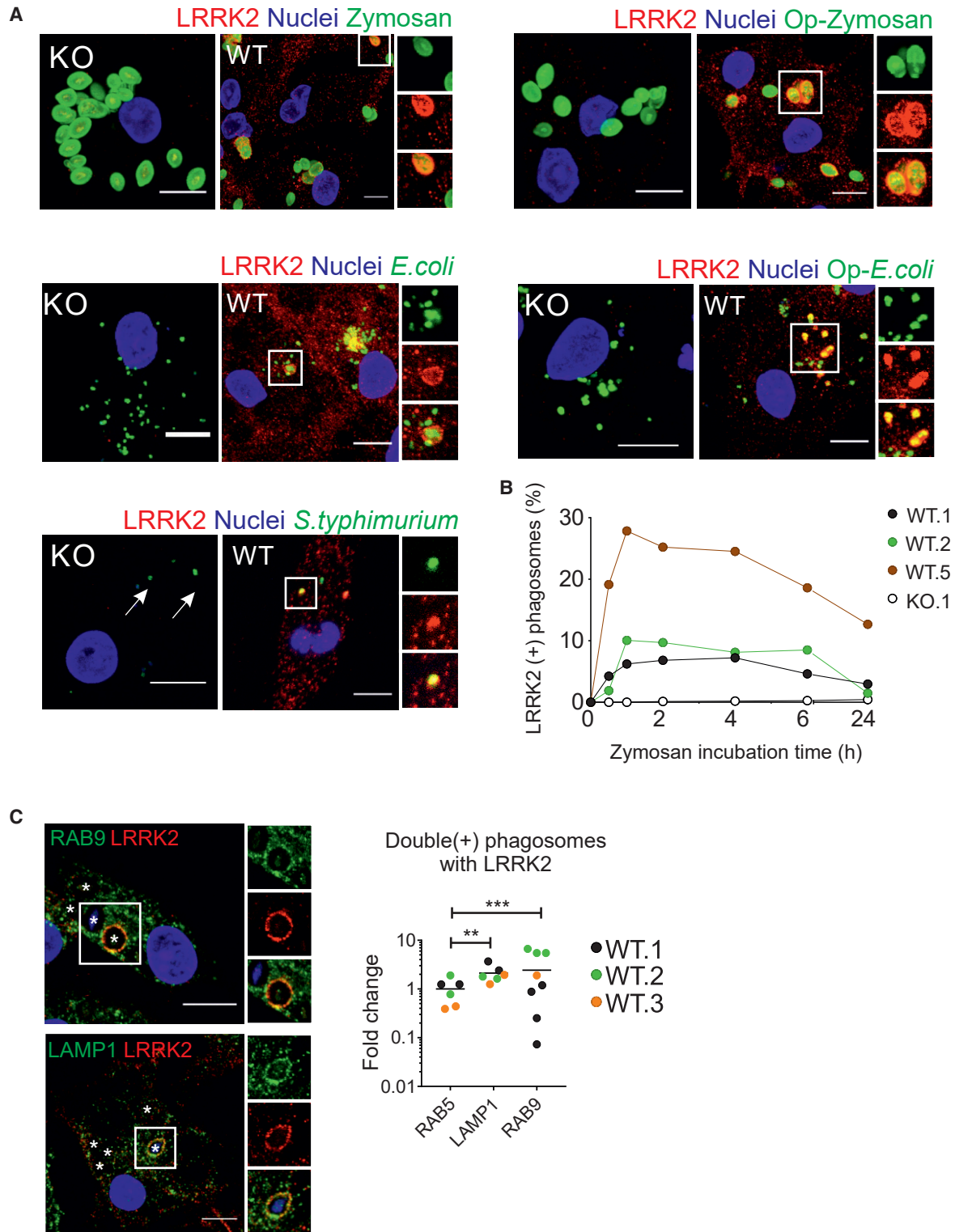


Figure 4. LRRK2 Is Recruited to Maturing Phagosomes

(A) Confocal images of LRRK2 WT and LRRK2 KO hiPSC macrophages fed with zymosan, immunoglobulin G (IgG)-opsonized zymosan (Op-Zymosan), *E. coli*, IgG-opsonized *E. coli* (Op-*E. coli*), GFP-expressing *S. typhimurium* (all Alexa Fluor 488 conjugated). Phagocytosis proceeded for 2 h before cells were fixed and stained with antibody against LRRK2. All scale bars represent 10 μ m.

(legend continued on next page)



clearly demonstrated the presence of LRRK2 on a subset of zymosan-containing phagosomes (in IFN- γ -treated cells to enable visualization of LRRK2) (Figure 4A). This was also observable with *Escherichia coli* bioparticles, with and without opsonization, and *Salmonella typhimurium* (Figure 4A). LRRK2 was not observed on phagosomes containing α syn fibrils, even when opsonized (Figure S5), indicating that LRRK2 recruitment is context dependent. The number of LRRK2-positive (LRRK2⁺) zymosan-containing phagosomes was time dependent, peaking at 1–2 h after addition of the meal to cells (mean 14.7%, range 6.8%–25.2% at 2 h), so 2-h zymosan incubation was used for all subsequent experiments (Figure 4B). LRRK2⁺ phagosomes were found to also be positive for the late phagosomal markers lysosome-associated protein LAMP-1 and RAB9, with significantly more LRRK2⁺LAMP-1⁺ or LRRK2⁺RAB9⁺ phagosomes than LRRK2⁺RAB5⁺ phagosomes (an early phagosome marker) (Figure 4C). Together, these data show that LRRK2 is recruited during later stages of phagosome maturation in hiPSC macrophages, around the time when lysosomes are recruited to phagosomes.

RAB8a and RAB10 Are Recruited to Phagosomes, and This Is LRRK2 Dependent

RAB GTPases regulate various fission and fusion events during phagocytosis, and in LRRK2-overexpression systems and non-human systems LRRK2 has been shown to associate physically with subsets of this family of proteins (Dodson et al., 2011; Gómez-Suaga et al., 2014; Steger et al., 2016; Waschbüsch et al., 2014; Yun et al., 2015). Importantly, several RABs, particularly RAB8a and RAB10, have been identified as physiological substrates of LRRK2, able to be phosphorylated by LRRK2 (on Thr72/73, respectively) (Fan et al., 2018; Steger et al., 2016). We therefore investigated whether these RAB GTPases are involved during LRRK2 recruitment to phagosomes. RAB8a and RAB10 could be observed coating the same phagosomes as LRRK2, while RAB7 had no significant association with LRRK2⁺ phagosomes (Figures 5A and 5B). 14-3-3 proteins, which associate with pS935-LRRK2 (Dzamko et al., 2010), did not appear closely co-localized with LRRK2 but could be observed just peripheral to LRRK2-coated clusters of phagosomes (not quantified). Importantly, the number of RAB8⁺ and RAB10⁺ phagosomes was significantly reduced (to back-

ground levels) in LRRK2 KO hiPSC macrophages (Figures 5A and 5C), and the number of phosphoT73 RAB10⁺ phagosomes was also significantly reduced (Figures 5D and 5E), demonstrating that the presence of LRRK2 is necessary for recruitment of RAB8a and RAB10 to phagosomes.

LRRK2 Kinase Inhibitors Increase LRRK2 Density at Phagosomes but Inhibit RAB8a and RAB10 Recruitment

In LRRK2-overexpressing HEK 293T cells, it has been reported that LRRK2 kinase inhibitors affect localization of LRRK2 within the cell, from diffused cytosolic distribution to more discrete cytosolic pools (Dzamko et al., 2010). Therefore, we investigated whether the application of LRRK2 kinase inhibitors would affect LRRK2 recruitment to phagosomes during phagocytosis. Pre-treating hiPSC macrophages with LRRK2 kinase inhibitors did not change the total number of LRRK2⁺ phagosomes. However, we noticed that significantly more (4-fold) of these LRRK2⁺ phagosomes displayed enhanced LRRK2 signal (referred to as “supercoated” LRRK2 phagosomes, LRRK2⁺⁺, Figures 6A–6C). This was also observable with the LRRK2 G2019S patient line and its isogenic control (Figures S6A and S6B). There was no significant difference between the isogenic pair of lines, suggesting that monoallelic G2019S LRRK2 kinase enhancement is not potent enough to give a detectable difference in “supercoating” compared with strong drug-induced kinase inhibition.

Although LRRK2 kinase inhibition led to an increase in LRRK2 presence at phagosomes, RAB8a and RAB10 colocalization at LRRK2⁺ phagosomes was reduced (Figures 6D, 6E, S6C, and S6D). This observation was also replicated in the G2019S isogenic pair (Figure S6E). Note that while kinase inhibition significantly reduced RAB8a and RAB10 recruitment, there was no significant difference between the G2019S line and its isogenic corrected line, implying again that this monoallelic mutation is subtle in relation to the effects of potent chemical inhibitors. Importantly, LRRK2 kinase inhibition also significantly reduced detection of phosphoRAB10 at phagosomes (Figures 6D and 6E). Together, these results show that although kinase inhibition causes LRRK2 to accumulate on phagosomes, without kinase activity LRRK2 cannot recruit RAB8a or RAB10.

(B) Quantification of LRRK2⁺ phagosomes over time. Each data point represents the percentage of total phagosomes that were LRRK2⁺ (by automated image analysis), mean of 20 random fields. Note that low absolute numbers of phagosomes earlier than 30 min precluded accurate LRRK2 quantification.

(C) hiPSC macrophages fed with zymosan bioparticles were stained with antibodies against LRRK2 and markers associated with maturing phagosomes, LAMP1 and RAB9. Internalized zymosan bioparticles are indicated by an asterisk to better visualize decoration of phagosome membrane by LRRK2 and marker staining. Bar graph shows fold change in the number of LRRK2⁺ phagosomes displaying late phagosomal markers versus early phagosome marker (RAB5). Two-way ANOVA with Dunnett’s multiple comparisons test was used for statistical analysis, **p < 0.01, ***p < 0.001.

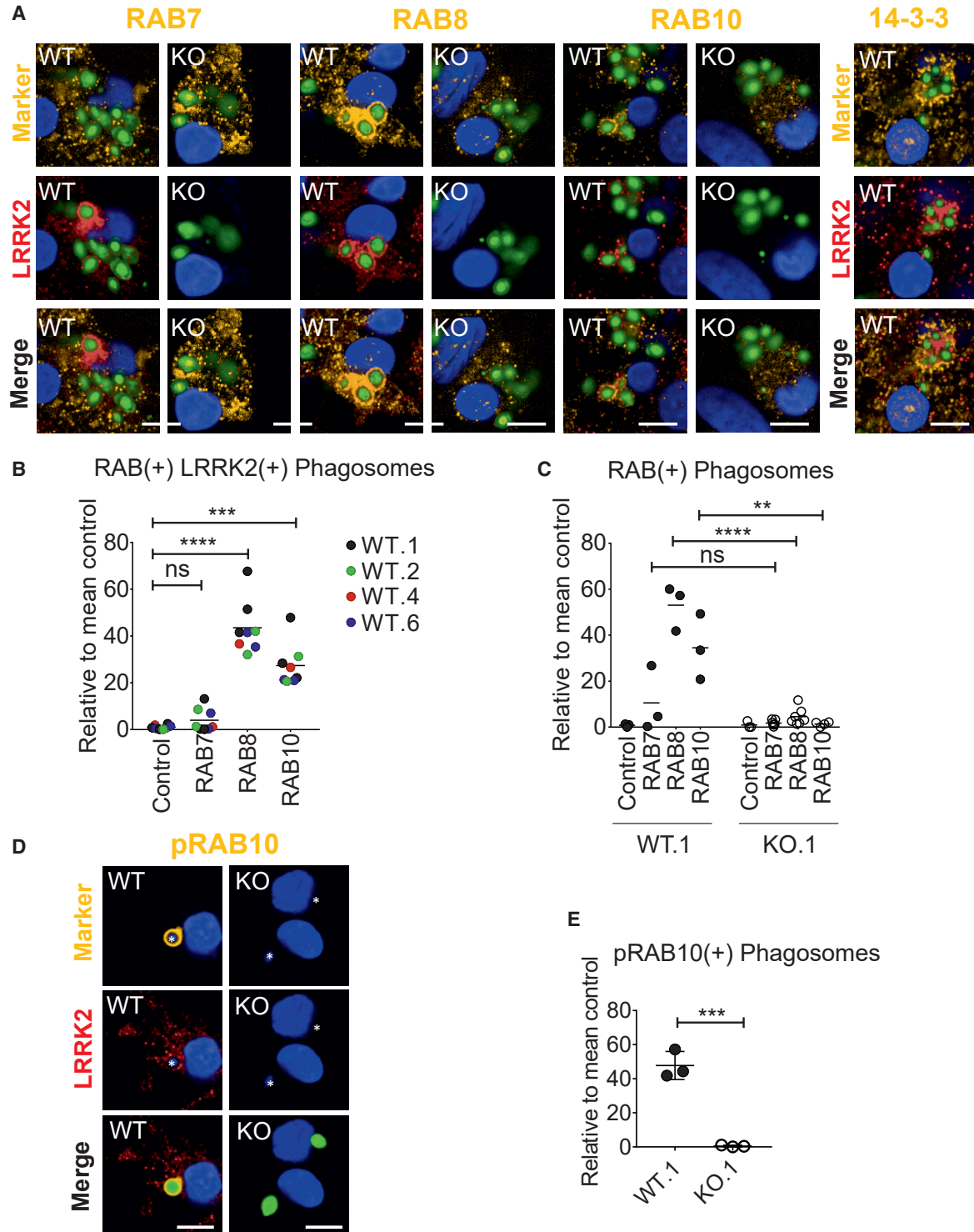


Figure 5. RAB8 and RAB10 Are Recruited to Phagosomes, and This Is LRRK2 Dependent

(A) Confocal images of LRRK2 WT and LRRK2 KO hiPSC macrophages fed with zymosan Alexa Fluor 488 for 2 h, then fixed and stained for LRRK2 (Alexa Fluor 647, red) and RABs (RAB10 D36C4) or pan-14-3-3 protein (Alexa Fluor 546, yellow). Scale bars represent 10 μ m.

(B) Quantification of number of LRRK2⁺ phagosomes that are also RAB⁺. Data from four WT hiPSC macrophage lines (WT.1, WT.2, WT.4, WT.6); each data point represents the mean of 20 fields per independent replicate. Control, secondary antibody only.

(legend continued on next page)



DISCUSSION

Here, we have characterized a platform for understanding LRRK2 function using hiPSC-derived macrophages and microglia, including gene-edited lines, which has enabled us to interrogate the involvement of LRRK2 in phagocytic processes in authentic, professional phagocytes.

While numerous studies have used hiPSC-derived neurons and astrocytes to study LRRK2 function (reviewed in Booth, 2017), the advantages of iPSC technology have barely begun to be applied to studying its function in the myeloid lineage. Our hiPSC macrophages have been used in one previous study as a validation of observations in mouse that *M. tuberculosis* survival inside macrophages requires LRRK2 (Härtlova et al., 2018). To our knowledge, only one other group has previously looked at LRRK2 in hiPSC-derived myeloid cells, describing an impact of the G2019S mutation on differentiation capacity (Speidel et al., 2016); however, we did not find this in our system over multiple differentiations with our G2019S isogenic pair or our LRRK2 KO isogenic pair.

We show that endogenous LRRK2 in hiPSC macrophages and microglia is strongly induced by immune signals, particularly IFN- γ , as reported in other systems (Gardet et al., 2010; Lee et al., 2017). This upregulation reveals additional bands by western blot, notably a prominent band running at ~170–187 kDa (predicted from proteomic analysis), possibly equivalent to the ~160-kDa truncated product reported by others in mouse kidney proximal tubule cells (also detectable in lung and spleen but not brain) (Herzig et al., 2011). Since it does not include S935, it appears not to correspond exactly to the ~200-kDa product reported in neutrophils and peripheral blood mononuclear cells (Fan et al., 2018). We have identified the LRRK2 cleavage region in hiPSC macrophages to be within the ANK-LRR interdomain region, likely more susceptible to cleavage, particularly if 14-3-3 proteins are not bound to the nearby S910/S935 phosphorylation sites. Structural modeling predicts that LRRK2 dimers have C-terminal (kinase and WD40) domains folded backward, in contact with N-terminal domains, suggesting that N-terminal domains may modulate enzymatic activity (Guaitoli et al., 2016). While this cleavage product could be merely the first stage of LRRK2 degradation, it could also, by lacking the N-terminal Armadillo/Ankyrin domains, affect LRRK2 cellular localization, kinase activity, and/or interaction with other proteins.

In our assays, LRRK2 did not impact on the initial uptake of phagocytic particles. Previous studies have yielded conflicting results regarding LRRK2 and phagocytic uptake. Small interfering RNA-mediated knockdown of LRRK2 has been variously reported to reduce phagocytic uptake in mouse microglial transformed BV-2 cells (Marker et al., 2012) and, conversely, to have no effect in mouse macrophage transformed RAW264.7 cells and BV-2 cells (Schapansky et al., 2014), nor in primary mouse LRRK2 KO microglia versus WT (Härtlova et al., 2018; Maekawa et al., 2016). A recent study across multiple systems (fly, mouse, and Parkinson's patients) has implicated LRRK2 in phagocytic uptake of beads or *E. coli* through LRRK2 phosphorylating the actin-remodeling complex component, WAVE2 (Kim et al., 2018). It is not clear why our results diverge from this study, as hiPSC macrophages express levels of WAVE2 similar to those of primary human monocytes and microglia (Haenseler et al., 2017a), but it may reflect technical differences (e.g., that study used serum-containing medium, which can lead to engagement of different receptor subsets; and *ex vivo* primary cells may reflect background donor physiological status) that could affect the engagement of the actin-remodeling complex and the relative impact of LRRK2 in the process (Rotty et al., 2017).

Our observations that in hiPSC macrophages LRRK2 is recruited to late phagosomes containing zymosan, *E. coli*, or *S. typhimurium*, extends the observation made by Gardet et al. (2010), who observed recruitment of LRRK2 to *S. typhimurium*-containing phagosomes in RAW264.7 cells. Zymosan engages Toll-like receptor 2 (TLR2) and dectin-1 receptors, *E. coli* engages TLR4, and *S. typhimurium* engages TLR2/TLR4. We did not observe LRRK2 recruitment to α -synuclein (α syn) fibrils under these experimental conditions. Oligomeric α syn engages TLR1/2, and monomeric α syn engages TLR4 (Fellner et al., 2013; Kim et al., 2012), but exactly which receptors α syn fibrils engage is currently unclear. The relationship between LRRK2 and aggregated α syn is not, therefore, as clear-cut as between LRRK2 and bacterial and fungal pathogens in this phagocytic context.

In our system, LRRK2 co-localizes with late phagocytic markers RAB9 and LAMP1 rather than with the early phagocytic marker RAB5, and also co-localizes with RAB8a and RAB10 but not with RAB7. RAB9 facilitates the recycling of mannose 6-phosphate receptors (M6PRs) between the phagosomes and the *trans*-Golgi network (TGN). M6PRs are important in delivering newly

(C) Quantification of RAB⁺ phagosomes; each data point represents the mean of 20 fields per independent replicate.

(D) Images as in (A) but stained for phosphoT73 RAB10 (Ab230261).

(E) Quantification of (D), each data point represents the mean of 20 fields per independent replicate, overall mean \pm SD.

One-way ANOVA with Tukey's multiple comparison was performed for all statistical analyses, **p < 0.01, ***p < 0.001, ****p < 0.0001, not significant, ns: p > 0.05.

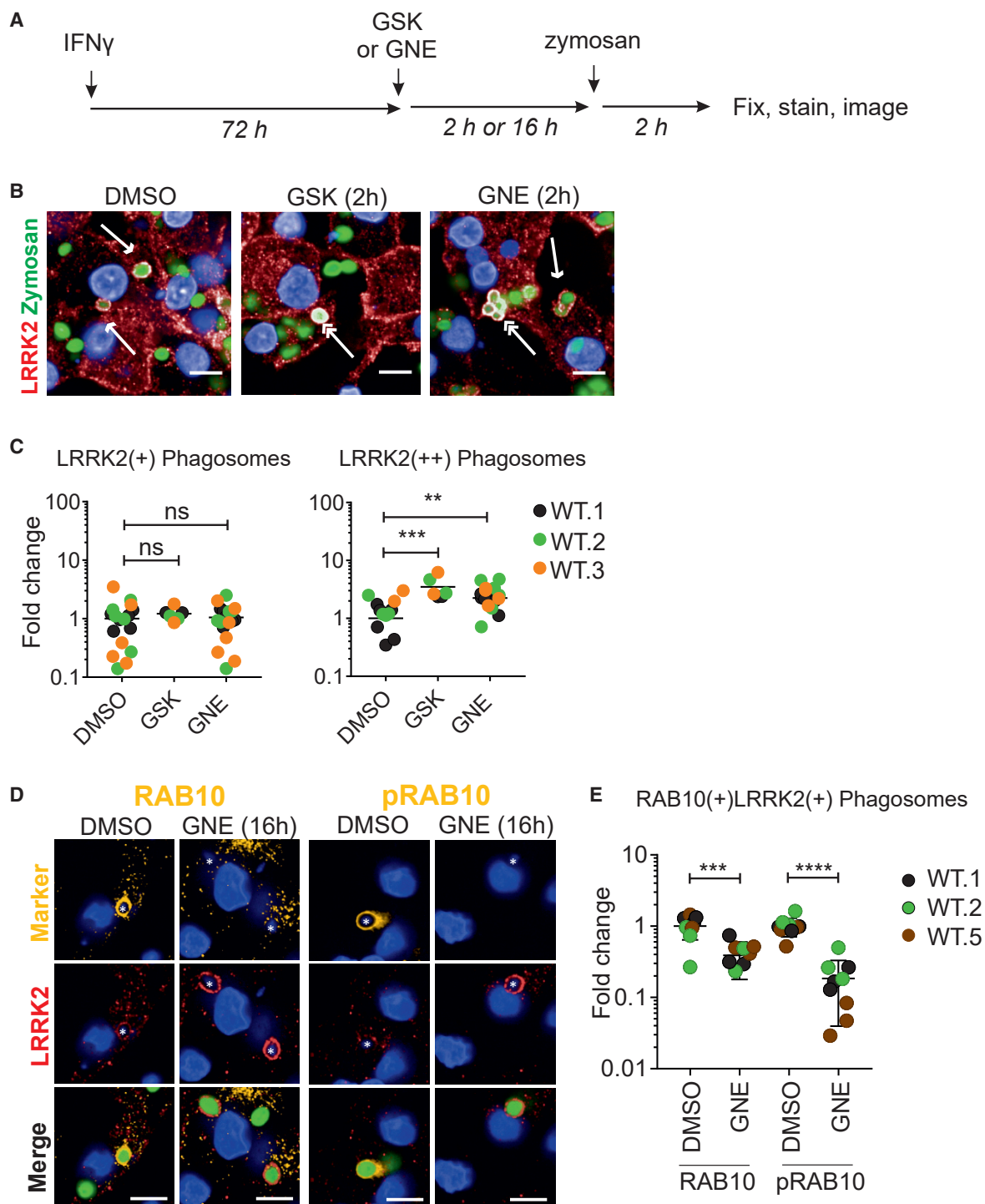


Figure 6. LRRK2 Kinase Inhibitors Increase LRRK2 Density at Phagosomes but Inhibit RAB8 and RAB10 Recruitment

(A) hiPSC macrophages were pre-treated with GSK (1 μ M) or GNE (1 μ M) for 2 h or 16 h before Alexa 488 zymosan bioparticles were added. Phagocytosis proceeded for 2 h, then cells were fixed and stained with antibody against LRRK2.

(B) Confocal images show examples of LRRK2⁺ phagosomes (single-headed arrows) and LRRK2⁺⁺ ("supercoated") phagosomes (double-headed arrows).

(C) Quantification of (B). Each dot shows data (mean) collected from at least 300 cells based on images acquired from at least five randomized fields. Two-way ANOVA with Fisher's least significant difference test was used for the statistical analysis.

(legend continued on next page)



synthesized lysosomal enzymes from the TGN to phagosomes (Riederer et al., 1994). LAMP-1, while found abundantly on lysosomes (Eskelinen et al., 2003), is recruited to phagosomes prior to RAB7 recruitment, which is required for the formation of phagolysosomes (Huynh et al., 2007). Therefore, it is conceivable that LRRK2 is recruited prior to recruitment of RAB7. RAB8a is involved in vesicle transport and membrane recycling to the cell surface (Banton et al., 2014), autophagy (with the amyotrophic lateral sclerosis-related gene, C9orf72, implicated as a RAB8 GEF) (Corbier and Sellier, 2017), and has previously been linked to LRRK2 in, variously, endolysosomal trafficking (Rivero-Ríos et al., 2019), centrosome function (Madero-Pérez et al., 2018), and ciliogenesis (Steger et al., 2017). RAB10 has been associated with TLR4 recycling to the surface from endosomes/Golgi (Wang et al., 2010) and has also been implicated in LRRK2-mediated ciliogenesis (Steger et al., 2017). Therefore, these RABs could be recruited by LRRK2 to maturing phagosomes in our system to participate in recycling/rerouting of phagocytosed membrane, receptors, and contents. Härtlova et al. (2018) implicate LRRK2 in retarding *M. tuberculosis* phagosome maturation. Combined with our findings here, it is conceivable that LRRK2 provides links to alternative fates for phagosomal components and contents other than a direct route to total proteolysis.

Steger et al. (2017) identified RABs as bona fide substrates of LRRK2, with RAB3A/B/C/D, RAB8A/B, RAB10, RAB12, RAB35, and RAB43 as the subset of RABs phosphorylated by LRRK2 in cells, and phosphorylation of RAB10 has been exploited as a readout of LRRK2 kinase activity in human neutrophils (Fan et al., 2018). We have demonstrated that RAB10, which co-localizes with LRRK2 at phagosomes and whose recruitment is dependent on LRRK2 presence and kinase activity, is phosphorylated by LRRK2 at this location. We have, therefore, extended the observations of Eguchi et al. (2018) in chloroquine-stressed mouse myeloid lines (briefly also noting LRRK2 recruitment to zymosan phagosomes) to show LRRK2-dependent RAB8a and RAB10 recruitment to phagosomes in authentic human macrophages, using phagocytosis of bioparticles as a physiologically relevant system rather than chemically induced lysosomal stress, and we have observed LRRK2 “supercoating” of phagosomes upon LRRK2 kinase inhibitor treatment. Accumulation of kinase-inhibited LRRK2 suggests that LRRK2 does not need kinase activity to be

recruited to phagosomes but needs to phosphorylate a substrate in order to leave the phagosome. Alternatively, it is possible that LRRK2 inhibitor-induced loss of S935 phosphorylation and 14-3-3 binding dictate supercoating rather than kinase activity per se, and might also explain the similar supercoating seen with the G2019S isogenic pair. iPSC macrophages harboring R1441 mutations (with increased kinase activity but reduced S935 phosphorylation) or edited to express S935A LRRK2 (with normal kinase activity) or kinase dead LRRK2 (still phosphorylated on S935) would resolve this open question.

Most papers studying LRRK2 function rely on biochemical approaches, western blot, and tagged or overexpressed constructs, which may not localize properly, due to tagging and/or overexpression leading to incorrect stoichiometry with other proteins. By optimizing staining for visualizing LRRK2 in hiPSC macrophages by confocal microscopy, we have been able to interrogate the translocation of endogenous, untagged LRRK2 within relevant human cells, revealing the point during phagosome maturation that LRRK2 recruits RAB8a and RAB10 and pointing to a possible role for LRRK2 in rerouting and recycling phagocytosed membrane, receptors, and contents.

EXPERIMENTAL PROCEDURES

Generation of LRRK2 Modified hiPSC Lines

The iPSC lines used in this paper were derived from dermal fibroblasts using non-integrating Sendai reprogramming vectors (Cytotune, Life Technologies), from donors recruited through StemBANCC (Morrison et al., 2015)/Oxford Parkinson's Disease Center: participants were recruited to this study having given signed informed consent, which included derivation of hiPSC lines from skin biopsies (Ethics Committee: National Health Service, Health Research Authority, NRES Committee South Central, Berkshire, UK, who specifically approved this part of the study [REC 10/H0505/71]). They are deposited in the European Bank for Induced Pluripotent Stem Cells, EBiSC, <https://cells.ebisc.org/> and listed in hPSCreg, <https://hpscereg.eu/>. See Table S1 for details of lines (Buskin et al., 2018; Dafinca et al., 2016; Fernandes et al., 2016; Haenseler et al., 2017b) and Figure S1 for relevant characterization data. Whole-exome sequencing revealed no deleterious LRRK2 mutations in any of the donor fibroblasts other than G2019S in the patient-derived line. iPSCs were maintained in mTeSR1 (STEMCELL Technologies) or E8 (Life Technologies), on hESC-qualified Matrigel-coated (Becton-Dickinson) or Geltrex-coated (Life Technologies) plates, and passaged as clumps with

(D) Confocal images show lack of recruitment of RAB10 (Ab181367) to LRRK2⁺⁺ phagosome in the presence of LRRK2-kinase inhibitor GNE (16 h), whereas DMSO control shows co-localization of the two proteins at phagosomes (left-hand panel); right-hand panel shows the same but for phosphoT73 RAB10 (Ab241060).

(E) Quantification of (D). Data from three independent hiPSC-derived macrophage lines; each data point represents the mean of 20 fields per independent replicate, with overall mean \pm SD, one-tailed unpaired t test with Welch's correction. (C) and (E) **p < 0.01, ***p < 0.001, ****p < 0.0001, not significant, ns: p > 0.05. (B) and (D) scale bars represent 10 μ m.



0.5 mM EDTA in PBS (Beers et al., 2012). Large-scale SNP-QCed frozen batches were used for experiments to ensure consistency.

Differentiation of Macrophages and Microglia from hiPSCs

Macrophages and microglia were differentiated using previously published protocols (Haenseler et al., 2017a; van Wilgenburg et al., 2013). See Table S3 for media compositions. In brief, embryoid bodies were generated in mTeSR medium with bone morphogenetic protein 4, vascular endothelial growth factor, and stem cell factor, then differentiated along a primitive myeloid pathway in T175 flasks in X-VIVO 15 medium with macrophage colony-stimulating factor (M-CSF) and interleukin-3 (IL-3). After about 3 weeks onward, macrophage precursors emerging into the supernatant were harvested, passed through a 40- μ m cell strainer, centrifuged for 5 min at 400 \times g, and further differentiated for 1 week into macrophages in X-VIVO 15 containing 100 ng/mL M-CSF, with a 50% medium change at day 4.

Dual SMAD inhibition was used to differentiate cortical neurons from hiPSCs, based on Shi et al. (2012). Day-43 cortical neurons were then co-cultured with macrophage precursors in microglia differentiation medium containing IL-34 granulocyte M-CSF and underwent 14 days of differentiation in co-culture as described by Haenseler et al. (2017a).

Quantification of LRRK2-Positive Phagosomes

For each experiment, 50,000 macrophage precursors were seeded and differentiated for 1 week in separate wells of an Ibidi 96-well μ -plate (Ibidi #89626). hiPSC macrophages were treated with IFN- γ (100 ng/mL) for 72 h to increase expression of endogenous LRRK2 prior to the addition of the phagocytic materials: Alexa Fluor 488-conjugated zymosan (Life Technologies #Z23373), Alexa Fluor 488-conjugated *Escherichia coli* (Life Technologies #E13231), and GFP-expressing *S. typhimurium* (Tocris, NCTC 12023, MM11-25). Oregon Green 488-conjugated α syn fibrils (gift from Dr Kelvin Luk, University of Pennsylvania) were prepared with endotoxin depletion according to the published methods, tested for endotoxin levels, and used at a final dilution of ≤ 0.01 EU/mL endotoxin (a level considered negligible) (Luk et al., 2007, 2009).

After 2 h, cells were washed, fixed, and stained as described above. Five to 20 z-stacked confocal images per well were acquired from randomized fields using an Opera Phenix High Content Screening System (PerkinElmer) with a 63 \times objective. Quantification of phagosomes was carried out by the Columbus Image Data Storage and Analysis System (CambridgeSoft). Detailed methods used for the analysis are described in Supplemental Information.

Flow-Cytometry Phagocytosis Assays

Uptake of bioparticles was quantitatively assessed by adding Alexa Fluor 488-conjugated zymosan bioparticles (Life Technologies #Z23373) to hiPSC macrophages (two bioparticles per cell) for 30 min at 37°C, followed by wash steps with PBS and trypan blue (250 μ g/mL in PBS) to quench non-internalized bioparticles. Cells were detached by TrypLE and gentle manual scraping, centrifuged at 400 \times g for 5 min, and fixed with 4% formaldehyde in PBS. Internalized zymosan particles were quantified using a Becton-

Dickinson FACSCalibur flow cytometer (BD Biosciences) and analyzed using FlowJo software.

Statistics

Statistical analysis was carried out with GraphPad Prism. All data are represented as mean \pm SEM of at least three independent experiments carried out by using cells collected from at least three independent differentiation batches unless stated otherwise. When comparing the means from multiple groups against one control group, one-way analysis of variance (ANOVA) with Dunnett's post hoc comparison or, for data not displaying normal distribution, non-parametrical Kruskal-Wallis with Dunnett's post hoc comparison were used, unless stated otherwise. Statistical significance is presented in the figures as * $p < 0.05$, ** $p < 0.01$, *** $p < 0.001$, **** $p < 0.0001$, and not significant (ns; $p > 0.05$).

SUPPLEMENTAL INFORMATION

Supplemental Information can be found online at <https://doi.org/10.1016/j.stemcr.2020.04.001>.

AUTHOR CONTRIBUTIONS

Conceptualization, H.L., W.S.J., and S.A.C.; Methodology, H.L., R.F., P.J.C., F.J.N., M.S., W.H., and S.A.C.; Investigation, H.L., R.F., I.S., E.H., and S.A.C.; Formal Analysis, H.L., I.S., E.H., and S.A.C.; Writing – Original Draft, H.L. and S.A.C.; Writing – Review & Editing, H.L., W.S.J., and S.A.C.; Funding Acquisition, R.W.-M., W.S.J., and S.A.C.; Resources, R.F., P.J.P., M.S., J.V., R.W.-M., W.S.J., and S.A.C.; Supervision, R.W.-M., W.S.J., and S.A.C.

ACKNOWLEDGMENTS

Financial support: The Wellcome Trust WT155121302 and the Oxford Martin School LC0910-004 (James Martin Stem Cell Facility Oxford, S.A.C.); the MRC Dementias Platform UK Stem Cell Network Capital Equipment MC_EX_MR/N50192X/1, Partnership MR/N013255/1 (R.W.-M., S.A.C.), and Momentum MC_PC_16034 (F.J.N., S.A.C.) Awards: ARUK Oxford Network pump-priming award (H.L.). The work was supported by the Innovative Medicines Initiative Joint Undertaking under grant agreement number 115439, resources of which are composed of financial contribution from the European Union's Seventh Framework Program (FP7/2007e2013) and EFPIA companies' in kind contribution (R.F.). We thank the High-Throughput Genomics Group at the Wellcome Trust Center for Human Genetics, Oxford (funded by Wellcome Trust grant reference 090532/Z/09/Z and MRC Hub grant G0900747 91070) for the generation of Illumina genotyping data. We would also like to thank the National Phenotypic Screening Center for instrument support. Funding, samples, and associated clinical data were supplied by the Oxford Parkinson's Disease Center study, funded by the Monument Trust Discovery award from Parkinson's UK, a charity registered in England and Wales (2581970) and in Scotland (SC037554), with the support of the National Institute for Health Research (NIHR) Oxford Biomedical Research Center based at Oxford University Hospitals NHS Trust and University of Oxford, and the NIHR Comprehensive Local Research Network (J.V., R.W.-M., S.A.C.).



Received: September 26, 2019

Revised: March 31, 2020

Accepted: April 1, 2020

Published: April 30, 2020

REFERENCES

- Atashrazm, F., Hammond, D., Perera, G., Bolliger, M.F., Matar, E., Halliday, G.M., Schüle, B., Lewis, S.J.G., Nichols, R.J., and Dzamko, N. (2019). LRRK2-mediated Rab10 phosphorylation in immune cells from Parkinson's disease patients. *Movement Disord.* **34**, 406–415.
- Banton, M.C., Inder, K.L., Valk, E., Rudd, C.E., and Schneider, H. (2014). Rab8 binding to immune cell-specific adaptor LAX facilitates formation of trans-golgi network-proximal CTLA-4 vesicles for surface expression. *Mol. Cell Biol.* **34**, 1486–1499.
- Beers, J., Gulbranson, D., George, N., Siniscalchi, L., Jones, J., Thomson, J., and Chen, G. (2012). Passaging and colony expansion of human pluripotent stem cells by enzyme-free dissociation in chemically defined culture conditions. *Nat. Protoc.* **7**, 2029–2040.
- Booth, H.D.E. (2017). *Modelling and Analysis of LRRK2 Mutations in iPSC-Derived Dopaminergic Neurons and Astrocytes* (University of Oxford).
- Buchrieser, J., James, W., and Moore, M. (2017). Human induced pluripotent stem cell-derived macrophages share ontogeny with MYB-independent tissue-resident macrophages. *Stem Cell. Rep.* **8**, 334–345.
- Buskin, A., Zhu, L., Chichagova, V., Basu, B., Mozaffari-Jovin, S., Dolan, D., Droop, A., Collin, J., Bronstein, R., Mehrotra, S., et al. (2018). Disrupted alternative splicing for genes implicated in splicing and ciliogenesis causes PRPF31 retinitis pigmentosa. *Nat. Commun.* **9**, 4234.
- Corbier, C., and Sellier, C. (2017). C9ORF72 is a GDP/GTP exchange factor for Rab8 and Rab39 and regulates autophagy. *Small GTPases* **8**, 181–186.
- Dafinca, R., Scaber, J., Ababneh, N.a., Lalic, T., Weir, G., Christian, H., Vowles, J., Douglas, A., Fletcher-Jones, A., Browne, C., et al. (2016). C9orf72 hexanucleotide expansions are associated with altered ER calcium homeostasis and stress granule formation in iPSC-derived neurons from patients with amyotrophic lateral sclerosis and frontotemporal dementia. *Stem cells* **34**, 2063–2078.
- Dodson, M.W., Zhang, T., Jiang, C., Chen, S., and Guo, M. (2011). Roles of the Drosophila LRRK2 homolog in Rab7-dependent lysosomal positioning. *Hum. Mol. Genet.* **21**, 1350–1363.
- Dzamko, N., Deak, M., Hentati, F., Reith, A., Prescott, A., Alessi, D., and Nichols, J. (2010). Inhibition of LRRK2 kinase activity leads to dephosphorylation of Ser(910)/Ser(935), disruption of 14-3-3 binding and altered cytoplasmic localization. *Biochem. J.* **430**, 405–413.
- EGUCHI, T., Kuwahara, T., Sakurai, M., Komori, T., Fujimoto, T., Ito, G., Yoshimura, S.-I., Harada, A., Fukuda, M., Koike, M., et al. (2018). LRRK2 and its substrate Rab GTPases are sequentially targeted onto stressed lysosomes and maintain their homeostasis. *Proc. Natl. Acad. Sci. United States America* **115**, E9115–E9124.
- Eskelinen, E.-L., Tanaka, Y., and Saftig, P. (2003). At the acidic edge: emerging functions for lysosomal membrane proteins. *Trends Cell Biol.* **13**, 137–145.
- Fan, Y., Howden, A., Sarhan, A., Lis, P., Ito, G., Martinez, T., Brockmann, K., Gasser, T., Alessi, D., and Sammler, E. (2018). Interrogating Parkinson's disease LRRK2 kinase pathway activity by assessing Rab10 phosphorylation in human neutrophils. *Biochem. J.* **475**, 23–44.
- Fellner, L., Irschick, R., Schanda, K., Reindl, M., Klimaschewski, L., Poewe, W., Wenning, G.K., and Stefanova, N. (2013). Toll-like receptor 4 is required for α -synuclein dependent activation of microglia and astroglia. *Glia* **61**, 349–360.
- Fernandes, H., Hartfield, E., Christian, H., Emmanouilidou, E., Zheng, Y., Booth, H., Bogetofte, H., Lang, C., Ryan, B., Sardi, P., et al. (2016). ER stress and autophagic perturbations lead to elevated extracellular α -synuclein in GBA-N370S Parkinson's iPSC-derived dopamine neurons. *Stem Cell. Rep.* **6**, 342–356.
- Ferreira, M., and Massano, J. (2017). An updated review of Parkinson's disease genetics and clinicopathological correlations. *Acta Neurol. Scand.* **135**, 273–284.
- Flynn, R., Grundmann, A., Renz, P., Hänseler, W., James, W., Cowley, S., and Moore, M. (2015). CRISPR-mediated genotypic and phenotypic correction of a chronic granulomatous disease mutation in human iPSC cells. *Exp. Hematol.* **43**, 838–848.
- Gardet, A., Benita, Y., Li, C., Sands, B., Ballester, I., Stevens, C., Korzenik, J., Rioux, J., Daly, M., Xavier, R., et al. (2010). LRRK2 is involved in the IFN-gamma response and host response to pathogens. *J. Immunol.* **185**, 5577–5585.
- Gómez-Suaga, P., Rivero-Ríos, P., Fdez, E., Blanca Ramírez, M., Ferrer, I., Aiastui, A., López De Munain, A., and Hilfiker, S. (2014). LRRK2 delays degradative receptor trafficking by impeding late endosomal budding through decreasing Rab7 activity. *Hum. Mol. Genet.* **23**, 6779–6796.
- Guañoli, G., Raimondi, F., Gilsbach, B.K., Gómez-Llorente, Y., Deyaert, E., Renzi, F., Li, X., Schaffner, A., Jagtap, P.K.A., Boldt, K., et al. (2016). Structural model of the dimeric Parkinson's protein LRRK2 reveals a compact architecture involving distant inter-domain contacts. *Proc. Natl. Acad. Sci.* **113**, E4357–E4366.
- Haenseler, W., Sansom, S., Buchrieser, J., Newey, S., Moore, C., Nicholls, F., Chintawar, S., Schnell, C., Antel, J., Allen, N., et al. (2017a). A highly efficient human pluripotent stem cell microglia model displays a neuronal-co-culture-specific expression profile and inflammatory response. *Stem Cell. Rep.* **8**, 1727–1742.
- Haenseler, W., Zambon, F., Lee, H., Vowles, J., Rinaldi, F., Duggal, G., Houlden, H., Gwinn, K., Wray, S., Luk, K., et al. (2017b). Excess α -synuclein compromises phagocytosis in iPSC-derived macrophages. *Scientific Rep.* **7**, 9003.
- Hakimi, M., Selvanantham, T., Swinton, E., Padmore, R., Tong, Y., Kabbach, G., Venderova, K., Girardin, S., Bulman, D., Scherzer, C., et al. (2011). Parkinson's disease-linked LRRK2 is expressed in circulating and tissue immune cells and upregulated following recognition of microbial structures. *J. Neural Transm.* **118**, 795–808.
- Härtlova, A., Herbst, S., Peltier, J., Rodgers, A., Bilkei-Gorzo, O., Fearn, A., Dill, B., Lee, H., Flynn, R., Cowley, S., et al. (2018).



LRRK2 is a negative regulator of Mycobacterium tuberculosis phagosome maturation in macrophages. *EMBO J.* 37, e98694.

Hatcher, J.M., Choi, H.G., Alessi, D.R., and Gray, N.S. (2017). Small-molecule inhibitors of LRRK2. In *Leucine-Rich Repeat Kinase 2 (LRRK2)*, H.J. Rideout, ed. (Springer International Publishing), pp. 241–264.

Herzig, M.C., Kolly, C., Persohn, E., Theil, D., Schweizer, T., Hafner, T., Stemmelen, C., Troxler, T.J., Schmid, P., Danner, S., et al. (2011). LRRK2 protein levels are determined by kinase function and are crucial for kidney and lung homeostasis in mice. *Hum. Mol. Genet.* 20, 4209–4223.

Hoeffel, G., and Ginhoux, F. (2015). Ontogeny of tissue-resident macrophages. *Front. Immunol.* 6, 486.

Huynh, K.K., Eskelinen, E.-L., Scott, C.C., Malevanets, A., Saftig, P., and Grinstein, S. (2007). LAMP proteins are required for fusion of lysosomes with phagosomes. *EMBO J.* 26, 313–324.

Karlsson, K., Cowley, S., Martinez, F., Shaw, M., Minger, S., and James, W. (2008). Homogeneous monocytes and macrophages from human embryonic stem cells following coculture-free differentiation in M-CSF and IL-3. *Exp. Hematol.* 36, 1167–1175.

Kim, B., Yang, M.-S., Choi, D., Kim, J.-H., Kim, H.-S., Seol, W., Choi, S., Jou, I., Kim, E.-Y., and Joe, E.-H. (2012). Impaired inflammatory responses in murine *Lrrk2*-knockdown brain microglia. *PLoS one* 7, e34693.

Kim, K.S., Marcogliese, P.C., Yang, J., Callaghan, S.M., Resende, V., Abdel-Messih, E., Marras, C., Visanji, N.P., Huang, J., Schlossmacher, M.G., et al. (2018). Regulation of myeloid cell phagocytosis by LRRK2 via WAVE2 complex stabilization is altered in Parkinson's disease. *Proc. Natl. Acad. Sci.* 115, E5164–E5173.

Lee, H., James, W., and Cowley, S. (2017). LRRK2 in peripheral and central nervous system innate immunity: its link to Parkinson's disease. *Biochem. Soc. Trans.* 45, 131–139.

Luk, K.C., Hyde, E.G., Trojanowski, J.Q., and Lee, V.M. (2007). Sensitive fluorescence polarization technique for rapid screening of alpha-synuclein oligomerization/fibrillization inhibitors. *Biochemistry* 46, 12522–12529.

Luk, K.C., Song, C., O'Brien, P., Stieber, A., Branch, J.R., Brunden, K.R., Trojanowski, J.Q., and Lee, V.M. (2009). Exogenous alpha-synuclein fibrils seed the formation of Lewy body-like intracellular inclusions in cultured cells. *Proc. Natl. Acad. Sci. U S A.* 106, 20051–20056.

Madero-Pérez, J., Fdez, E., Fernández, B., Lara Ordóñez, A., Blanca Ramírez, M., Gómez-Suaga, P., Waschbüsch, D., Lobbstaël, E., Baelkandt, V., Nairn, A., et al. (2018). Parkinson disease-associated mutations in LRRK2 cause centrosomal defects via Rab8a phosphorylation. *Mol. neurodegeneration* 13, 3.

Maekawa, T., Sasaoka, T., Azuma, S., Ichikawa, T., Melrose, H.L., Farrer, M.J., and Obata, F. (2016). Leucine-rich repeat kinase 2 (LRRK2) regulates α -synuclein clearance in microglia. *BMC Neurosci.* 17, 77.

Marker, D., Puccini, J., Mockus, T., Barbieri, J., Lu, S.-M., and Gelbard, H. (2012). LRRK2 kinase inhibition prevents pathological microglial phagocytosis in response to HIV-1 Tat protein. *J. neuroinflammation* 9, 261.

Moehle, M., Webber, P., Tse, T., Sukar, N., Standaert, D., DeSilva, T., Cowell, R., and West, A. (2012). LRRK2 inhibition attenuates microglial inflammatory responses. *J. Neurosci.* 32, 1602–1611.

Morrison, M., Klein, C., Clemann, N., Collier, D., Hardy, J., Heisserer, B., Cader, Z., Graf, M., and Kaye, J. (2015). StemBANCC: governing access to material and data in a large stem cell research Consortium. *Stem Cell. Rev.* 11, 681–687.

Ran, A., Hsu, P., Lin, C.-Y., Gootenberg, J., Konermann, S., Trevino, A., Scott, D., Inoue, A., Matoba, S., Zhang, Y., et al. (2013). Double nicking by RNA-guided CRISPR Cas9 for enhanced genome editing specificity. *Cell* 154, 1380–1389.

Riederer, M.A., Soldati, T., Shapiro, A.D., Lin, J., and Pfeffer, S.R. (1994). Lysosome biogenesis requires Rab9 function and receptor recycling from endosomes to the trans-Golgi network. *J. Cell Biol.* 125, 573–582.

Rivero-Ríos, P., Romo-Lozano, M., Madero-Pérez, J., Thomas, A.P., Bioss, A., Greggio, E., and Hilfiker, S. (2019). The G2019S variant of leucine-rich repeat kinase 2 (LRRK2) alters endolysosomal trafficking by impairing the function of the GTPase RAB8A. *J. Biol. Chem.* 294, 4738–4758.

Rotty, J.D., Brighton, H.E., Craig, S.L., Asokan, S.B., Cheng, N., Ting, J.P., and Bear, J.E. (2017). Arp2/3 complex is required for macrophage integrin functions but is dispensable for FcR phagocytosis and in vivo motility. *Dev. Cell* 42, 498–513.e6.

Schapansky, J., Nardozi, J., Felizia, F., and LaVoie, M. (2014). Membrane recruitment of endogenous LRRK2 precedes its potent regulation of autophagy. *Hum. Mol. Genet.* 23, 4201–4214.

Shi, Y., Kirwan, P., Smith, J., Robinson, H., and Livesey, F. (2012). Human cerebral cortex development from pluripotent stem cells to functional excitatory synapses. *Nat. Neurosci.* 15, 477–486.

Speidel, A., Felk, S., Reinhardt, P., Sternecker, J., and Gillardon, F. (2016). Leucine-rich repeat kinase 2 influences fate decision of human monocytes differentiated from induced pluripotent stem cells. *PLoS ONE* 11, e0165949.

Steger, M., Diez, F., Dhekne, H., Lis, P., Nirujogi, R., Karayel, O., Tonelli, F., Martinez, T., Lorentzen, E., Pfeffer, S., et al. (2017). Systematic proteomic analysis of LRRK2-mediated Rab GTPase phosphorylation establishes a connection to ciliogenesis. *eLife* 6, e31012.

Steger, M., Tonelli, F., Ito, G., Davies, P., Trost, M., Vetter, M., Wachter, S., Lorentzen, E., Duddy, G., Wilson, S., et al. (2016). Phosphoproteomics reveals that Parkinson's disease kinase LRRK2 regulates a subset of Rab GTPases. *eLife* 5, e12813.

Thévenet, J., Pescini Gobert, R., Hooft van Huijsduijn, R., Wiessner, C., and Sagot, Y.J. (2011). Regulation of LRRK2 expression points to a functional role in human monocyte maturation. *PLoS one* 6, e21519.

van Wilgenburg, B., Browne, C., Vowles, J., and Cowley, S. (2013). Efficient, long term production of monocyte-derived macrophages from human pluripotent stem cells under partly-defined and fully-defined conditions. *PLoS One* 8, e71098.

Wang, D., Lou, J., Ouyang, C., Chen, W., Liu, Y., Liu, X., Cao, X., Wang, J., and Lu, L. (2010). Ras-related protein Rab10 facilitates TLR4 signaling by promoting replenishment of TLR4 onto the plasma membrane. *Proc. Natl. Acad. Sci.* 107, 13806–13811.



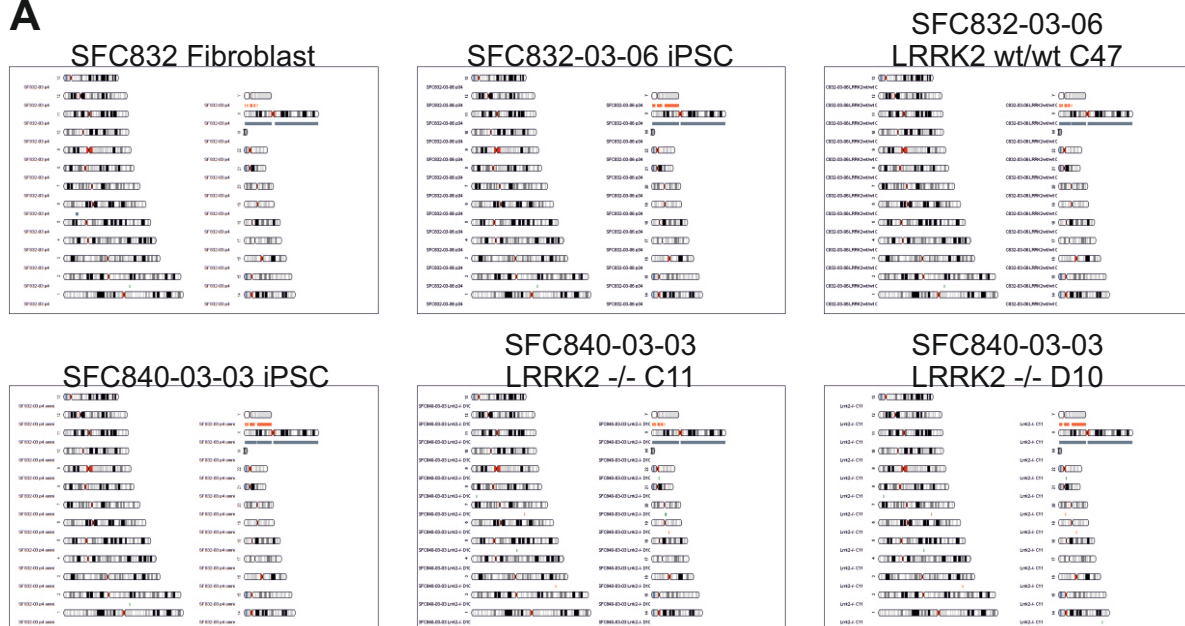
- Wang, D., Xu, L., Lv, L., Su, L.Y., Fan, Y., Zhang, D.F., Bi, R., Yu, D., Zhang, W., Li, X.A., et al. (2015). Association of the LRRK2 genetic polymorphisms with leprosy in Han Chinese from Southwest China. *Genes Immun.* 16, 112–119.
- Wang, Z., Arat, S., Magid-Slav, M., and Brown, J. (2018). Meta-analysis of human gene expression in response to *Mycobacterium tuberculosis* infection reveals potential therapeutic targets. *BMC Syst. Biol.* 12, 3.
- Waschbüsch, D., Michels, H., Strassheim, S., Ossendorf, E., Kessler, D., Gloeckner, C.J., and Barnekow, A. (2014). LRRK2 transport is regulated by its novel interacting partner Rab32. *PLOS ONE* 9, e111632.
- Witoelar, A., Jansen, I., Wang, Y., Desikan, R., Gibbs, R., Blauwendraat, C., Thompson, W., Hernandez, D., Djurovic, S., Schork, A., et al. (2017). Genome-wide pleiotropy between Parkinson disease and autoimmune diseases. *JAMA Neurol.* 74, 780–792.
- Wolf, S., Boddeke, H.W., and Kettenmann, H. (2017). Microglia in physiology and disease. *Annu. Rev. Physiol.* 79, 619–643.
- Yun, H.J., Kim, H., Ga, I., Oh, H., Ho, D.H., Kim, J., Seo, H., Son, I., and Seol, W. (2015). An early endosome regulator, Rab5b, is an LRRK2 kinase substrate. *J. Biochem.* 157, 485–495.
- Zhang, F.-R., Huang, W., Chen, S.-M., Sun, L.-D., Liu, H., Li, Y., Cui, Y., Yan, X.-X., Yang, H.-T., Yang, R.-D., et al. (2009). Genome-wide association study of leprosy. *New Engl. J. Med.* 361, 2609–2618.

Supplemental Information

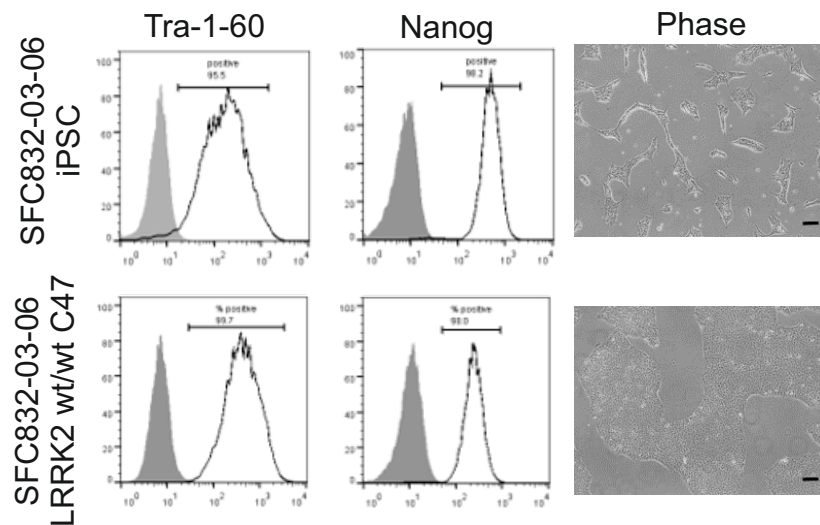
**LRRK2 Is Recruited to Phagosomes and Co-recruits RAB8 and RAB10
in Human Pluripotent Stem Cell-Derived Macrophages**

Heyne Lee, Rowan Flynn, Ishta Sharma, Emma Haberman, Phillippa J. Carling, Francesca J. Nicholls, Monika Stegmann, Jane Vowles, Walther Haenseler, Richard Wade-Martins, William S. James, and Sally A. Cowley

A



B



C

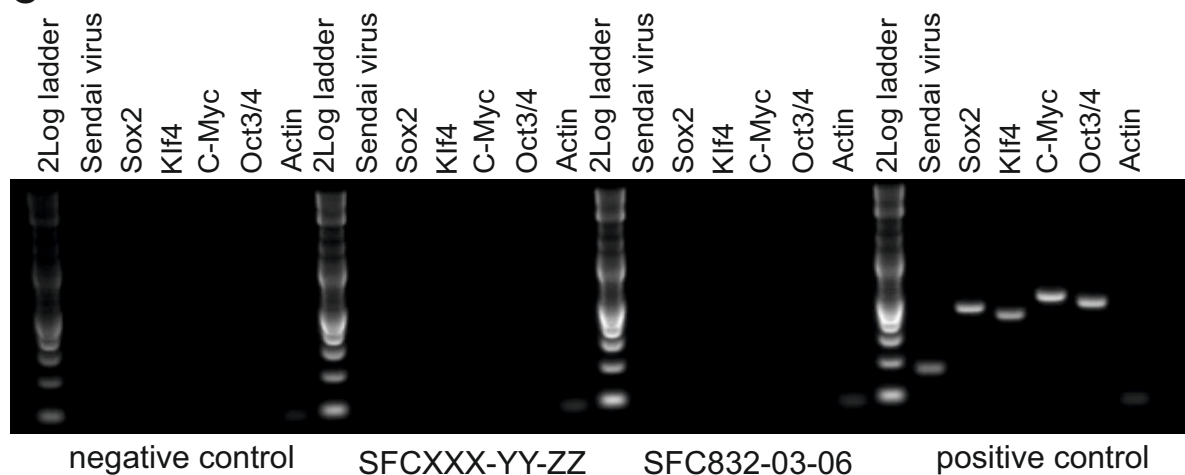


Figure S1. Quality control of hiPSC lines used in this study (related to Figure 1 and to Experimental procedures, Generation of LRRK2 modified hiPSC lines).

HiPSC line SFC832-03-06 and gene-edited lines characterised in this manuscript. (A) Genome integrity of SFC832-03-06 and gene-edited lines, assessed by Illumina Human CytoSNP12v2.1 or OmniExpress24 SNP array. Karyograms (KaryoStudio, Illumina) show amplifications (green)/deletions (orange)/LOH regions (grey) alongside the relevant chromosome (NB two X chromosomes annotated grey, Y chromosome orange, with poor coverage by CytoSNP12v2.1 versus OmniExpress24). (B) FACS analysis confirms expression of pluripotency markers Tra-1-60 and Nanog; open black plot represents antibody, filled grey plot is isotype control; Right-hand panel shows expected hiPSC colony morphology (phase-contrast microscopy), Scale bar, 100 μ m. (C) Clearance of Cytotune1 Sendai vectors from SFC832-03-06 (Log2 ladder; Sendai backbone 181bp; Sox2 451 bp; Klf4 410 bp; c-myc 532 bp; Oct-4 483 bp; β -actin control 92 bp; + control is fibroblasts infected with Cytotune 5 d previously).

A WT TCTGTCCAAGGTACAATGCAAAGCTTAATGGGACCCCAGGATGTTGGAAATGATGGGAAGT

Δ 16bp TCTGTCCAAGGTACAATGCAAAG-----GATGTTGGAAATGATGGGAAGT

+ 37bp TCTGTCCAAGGTACAATGCAAAGCTTAATGGGACCCCAGGATGTTGGAAATGATGGGAAGT

Clone D10 KO.1 ACAATGCAAAGCTTAATGGGACCCCAGGATGTTGGAA

WT TCTGTCCAAGGTACAATGCAAAGCTTAATGGGACCCCAGGATGTTGGAAATGATGGGAAGT

Δ 11bp TCTGTCCAAGGTACAATGCAA-----CCCCAGGATGTTGGAAATGATGGGAAGT

Δ 26bp TCTGTCCAAGGTACAATGCAAAGCTTAATGGGA-----AGT

Clone C11 KO.2

B MΦ precursor production curve

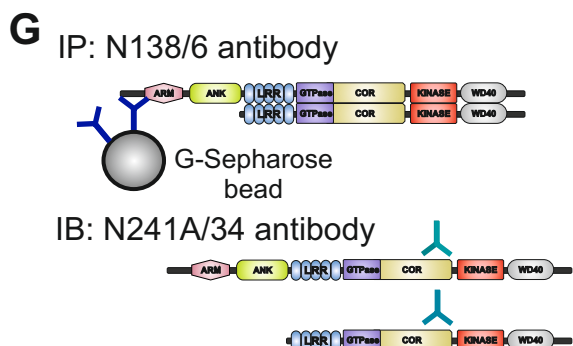
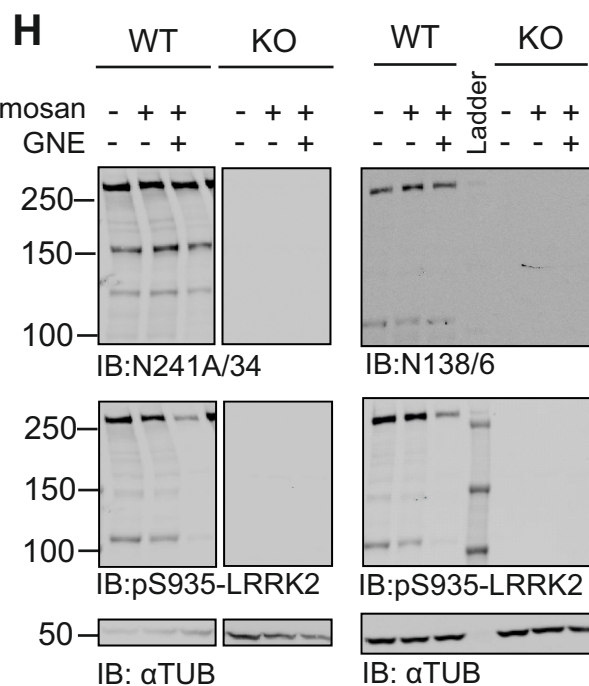
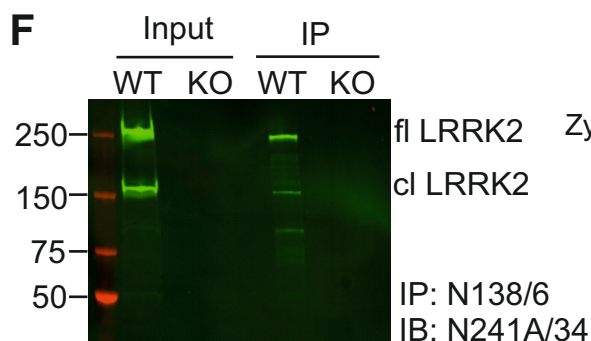
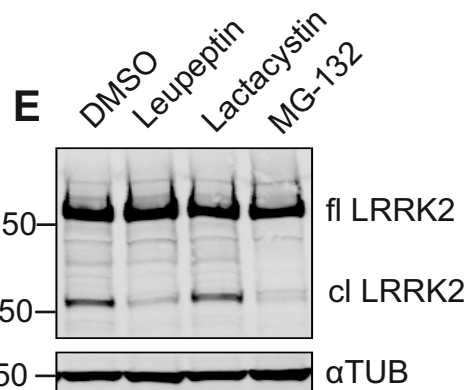
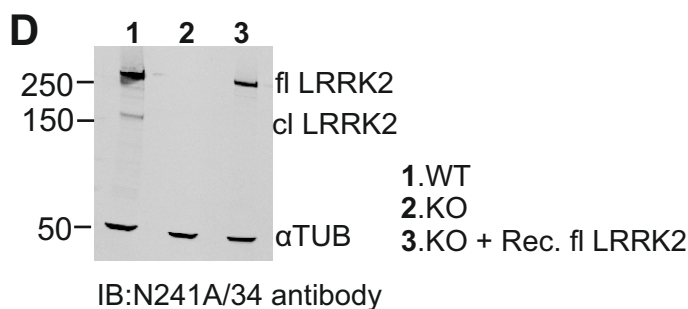
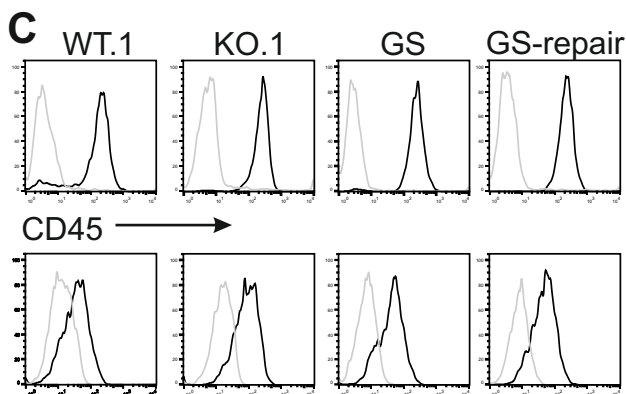
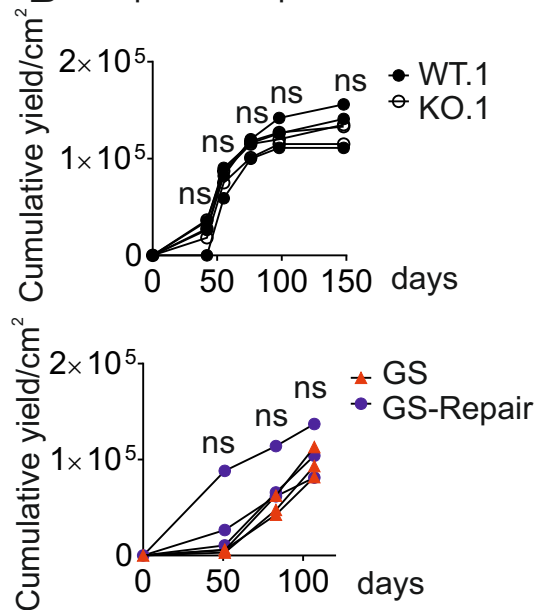


Figure S2. Differentiation of LRRK2 gene-edited hiPSC to macrophages and analysis of LRRK2 species (related to Figure 1).

(A) Sequences of each allele of hiPSC clones with CRISPR/Cas9-mediated double-allelic knockout of LRRK2. Black triangle indicates position of an inserted sequence. (B) Cumulative yield of macrophage precursors harvested from the supernatant of hiPSC-macrophage differentiation cultures, for final plating for mature macrophages. Each line represents an independent differentiation. Two-way ANOVA with Bonferroni multiple comparisons test was used for statistical analysis. (C) Flow cytometry of macrophage precursor cells from LRRK2 gene-edited hiPSC lines, for key myeloid markers CD45 and CD14. (D) Western blot of hiPSC-macrophage whole-cell lysate probed with C-terminal antibody for LRRK2 and with final column of LRRK2 KO macrophage lysate spiked with recombinant LRRK2, demonstrating lack of degradation of the recombinant protein in the experimental cell lysis conditions used in this study. (E) Western blot of whole cell lysates of hiPSC-macrophages incubated with protease inhibitors, probed with C-terminal LRRK2 antibody N241A/34. (F) Western blot of immunoprecipitation of LRRK2 from hiPSC-macrophages using N-terminal antibody, and probed with C-terminal antibody, showing co-precipitation of C-terminal truncated product. D-H, all with 72 h IFN γ activation. (G) Graphic showing the immunoprecipitation and blotting strategy in (F). (H) Western blot of Control (WT) and LRRK2 KO hiPSC-macrophage whole cell lysate probed with antibodies to C-terminal LRRK2 (N241A/34) and to pS935 LRRK2 (Left panel) or with antibodies to N-terminal LRRK2 (N138/6) and pS935 LRRK2, showing correspondence of the pS935 band with an N-terminal ~110kD band and not detectably with the C-terminal ~170kD band. α TUB loading controls are shown in D, E and H.

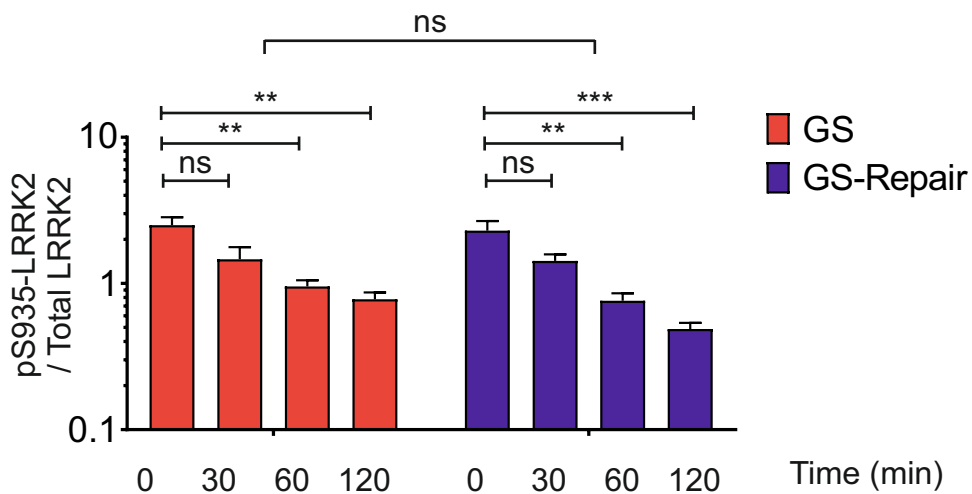
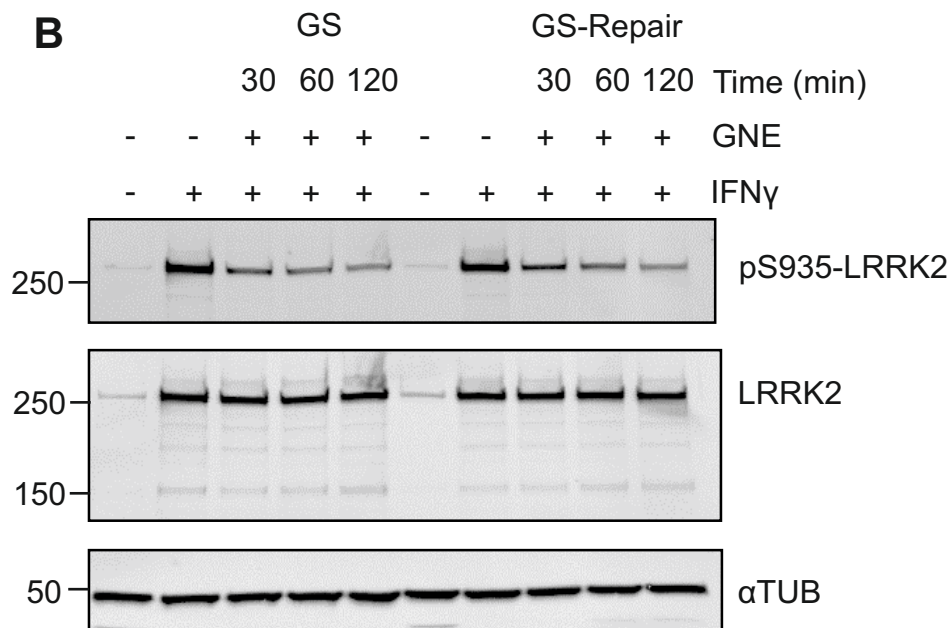
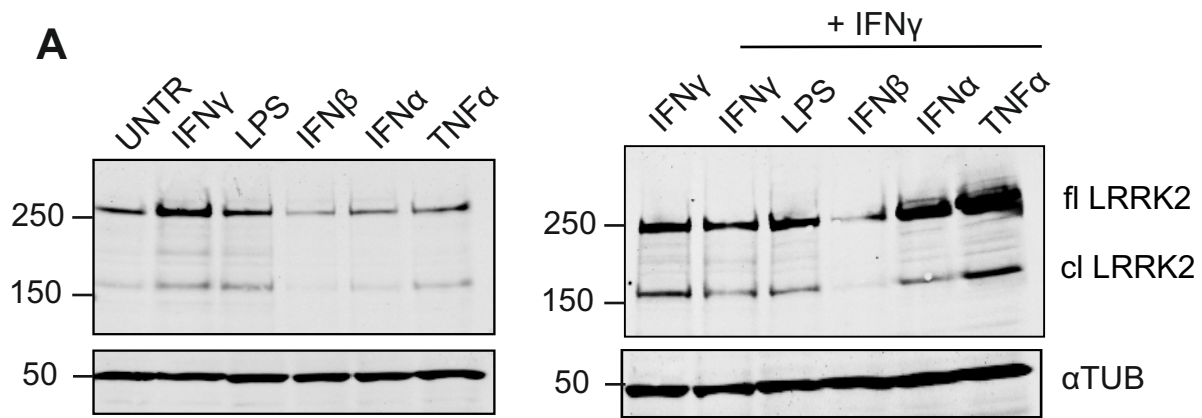


Figure S3. LRRK2 protein expression in activated hiPSC-macrophages, and with LRRK2 kinase inhibition (related to Figures 2 and 3).

(A) Western blot of hiPSC-macrophage whole-cell lysates following 72 h activation as indicated, probed with C-terminal LRRK2 antibody N241A/34. (B) As (A), for the LRRK2 G2019S and corrected isogenic cell line pair, with activation with IFN γ and incubation with LRRK2 kinase inhibitor GNE for 2 hours prior to cell lysis, plus additional WB probing with antibody for pS935 LRRK2. Lower panel, quantification of above, with mean and SEM of 3 experiments. Statistical analysis, 1-way ANOVA

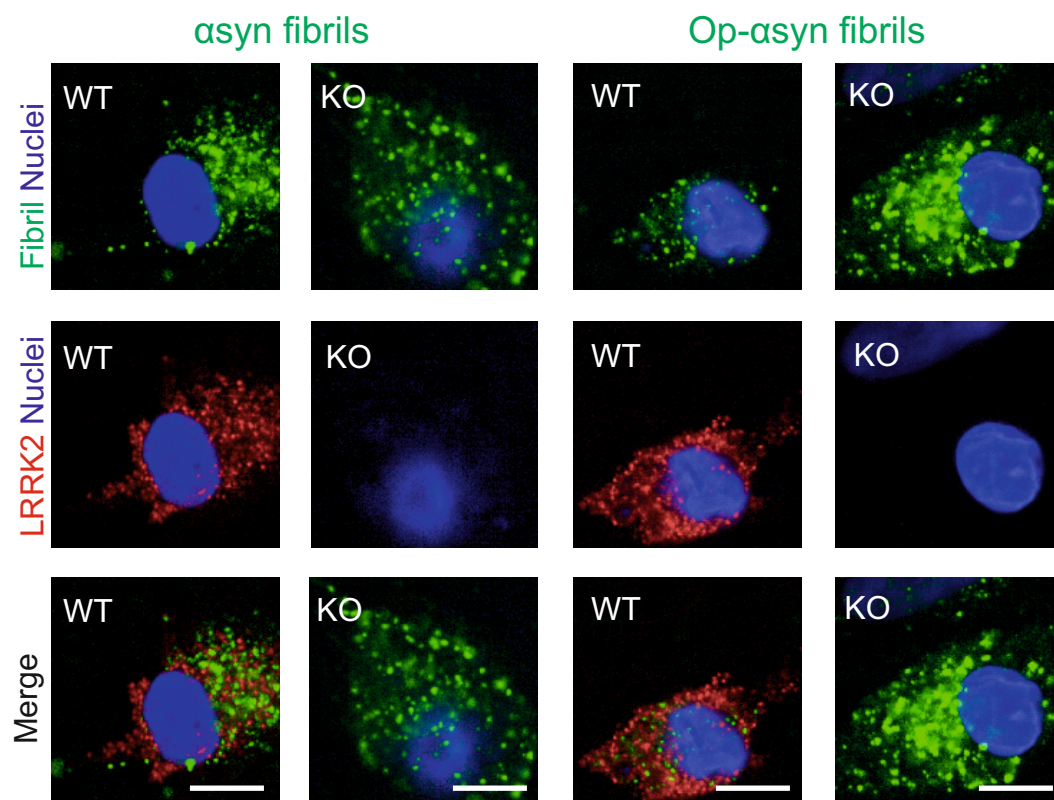


Figure S5. Additional phagocytic meal LRRK2-localisation data (related to Figure 4).

(A) Confocal images of hiPSC-macrophages following uptake of α -synuclein fibrils (Alexa-488 labelled, with and without opsonisation with pooled human serum), stained for LRRK2 (Alexa-647, red). Scale bar, 10 μ m.

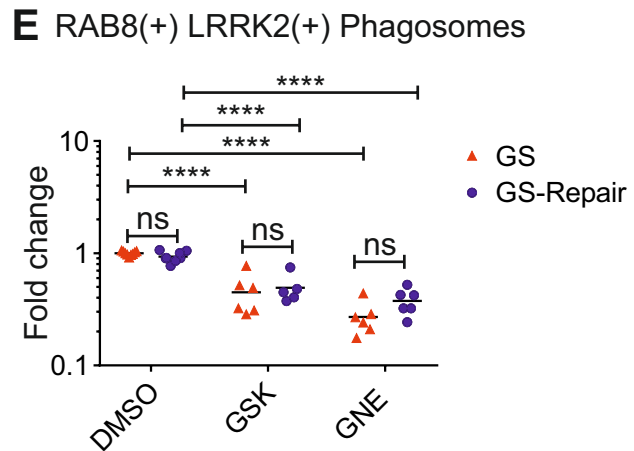
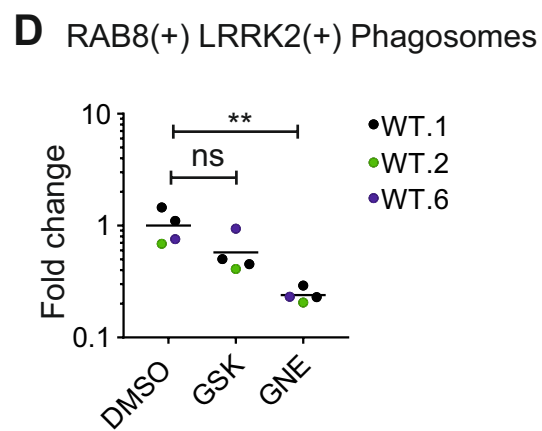
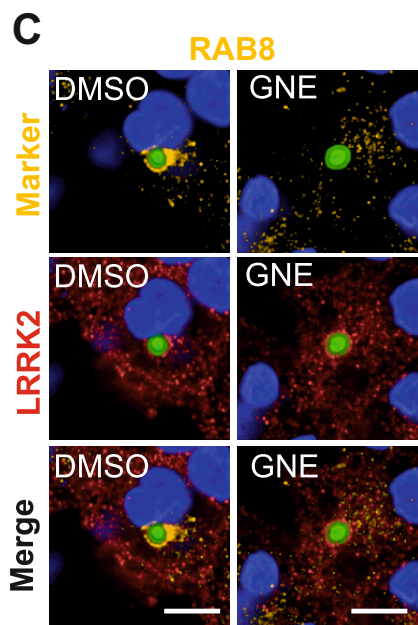
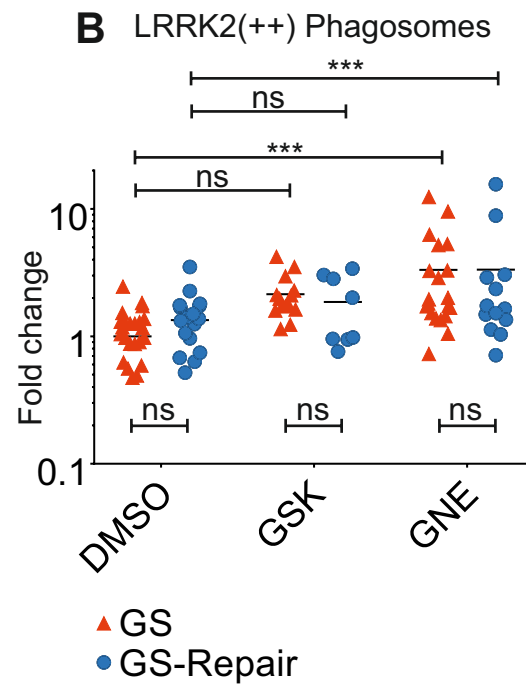
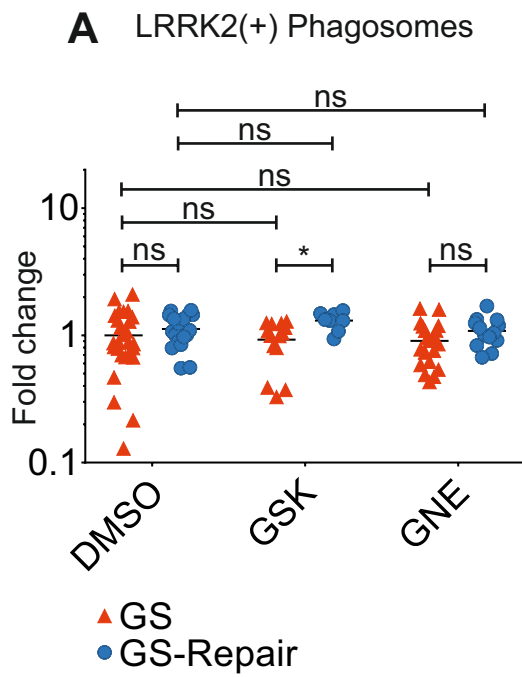


Figure S6. LRRK2 and RAB8 recruitment to hiPSC-macrophage phagosomes with LRRK2 kinase inhibition in WT and LRRK2 G2019S isogenic pair (related to Figure 6).

(A) Quantification of number of LRRK2(+) phagosomes in LRRK2 G2019S isogenic pair, as in Figure 6C. (B) As (A) but LRRK2(++) ('supercoated') phagosomes. Each data point represents the mean of 20 fields per independent replicate, 1-way ANOVA, Dunnett's post-hoc comparison. (C) Confocal images show lack of recruitment of RAB8 to LRRK2(++) phagosome in the presence of LRRK2-kinase inhibitor GNE (right-hand panel), whereas DMSO control shows colocalisation of the two proteins at phagosomes (left-hand panel). (D) Quantification of effect of LRRK2 kinase inhibitors GSK and GNE on recruitment of RAB8 to LRRK2(+) phagosomes. Data from 3 independent hiPSC-derived macrophage lines, each data point represents the mean of 20 fields per independent replicate, 1-way ANOVA, Dunnett's post-hoc comparison. (E) As (D) but data from GS and GS-repair isogenic hiPSC-macrophages.

Table S1. Human iPSC lines.

Labels		ID of fibroblast	ID of iPSC clone	Diagnosis	Genotype LRRK2	Gender	Age of Biopsy (years)	Repro-gramming method	PMID
WT.1	●	SFC840	SFC840-03-03	Healthy	WT/WT	F	67	Cytotune1	26905200
WT.2	●	SFC856	SFC856-03-04	Healthy	WT/WT	M	78	Cytotune2	28827786
WT.3	●	SBAD2	SBAD2-01	Healthy	WT/WT	M	51	Cytotune1	30315276
WT.4	●	SFC180	SFC180-01-01	Healthy	WT/WT	F	60	Cytotune2	28827786
WT.5	●	SFC841	SFC841-03-01	Healthy	WT/WT	M	36	Cytotune1	27097283
WT.6	●	SFC854	SFC854-03-02	Healthy	WT/WT	M	72	Cytotune2	28827786
KO.1	○	SFC840	SFC840-03-03 LRRK2 ^{-/-} D10	CRISPR/ Cas-9 edited	-/-				29789389 uses this clone; This paper for characterisation data
KO.2	○	SFC840	SFC840-03-03 LRRK2 ^{-/-} C11	CRISPR/ Cas-9 edited	-/-				This paper
GS	▲	SFC832	SFC832-03-06	PD	G2019S/WT	F	77	Cytotune1	This paper
GS-Repair	●	SFC832	SFC832-03-06 LRRK2 ^{WT/WT} C47	CRISPR/ Cas-9 edited	WT/WT				This paper

Table S2. Guide RNA sequences.

	Sequences 5' – 3'
LRRK2 KO gRNA oligo1	CACCGATTAAGCTTTGCATTGTACC
LRRK2 KO gRNA oligo2	AAACGGTACAATGCAAAGCTTAATC
LRRK2 KO gRNA oligo1	CACCGCCCAGGATGTTGGAAATGAT
LRRK2 KO gRNA oligo2	AAACATCATTTCACATCCTGGGC
LRRK2 G2019S Repair gRNA oligo 1	CACCGTCAGCAATCTTTGCAATGA
LRRK2 G2019S Repair gRNA oligo 2	AAACTCATTCGAAAGATTGCTGAC
LRRK2 G2019S Repair gRNA oligo 1	CACCGTCAGTACTGCTGTAGAATG
LRRK2 G2019S Repair gRNA oligo 2	AAACCATTCTACAGCAGTACTGAC

Table S3. Differentiation media.

Media	Composition
Macrophage differentiation	
EB differentiation medium	mTeSR (StemCell Technologies, 12491), 50 ng/mL BMP4 (Gibco, PHC9534), 50 ng/mL VEGF (PeproTech, 100-20), 20 ng/mL SCF (Miltenyi Biotec, 130-094-303)
Factory medium	X-VIVO-15 (Lonza, BE04-418F), 100 ng/mL M-CSF (Gibco, PHC9501), 25 ng/mL IL-3 (Gibco, PHC0033), 2 mM Glutamax, (Gibco 35050035) 100U/mL P/S, 0.055 mM 2-ME
Macrophage differentiation medium	X-VIVO-15, 100 ng/mL M-CSF, 2 mM Glutamax, 100 U/mL P/S, 0.055 mM 2-ME
Microglia-cortical neuron co-culture	
Neural induction medium	Neural maintenance medium, 10 μ M SB431542 (Tocris, 1614), 1 μ M Dorsomorphin (Tocris, 3093)
Neural maintenance medium	50:50 mix: DMEM F12 (Gibco, 21331020) supplemented 1 in 100 N2 (Gibco, 17502048), 2 mM Glutamax and Neurobasal medium (Gibco, 21103049) supplemented 1 in 50 B27 (Gibco, 17504044), 2 mM Glutamax
Microglia-neuron co-culture medium	Advanced DMEM F12 (Gibco, 12634010), 1 in 100 N2, 100 ng/mL IL-34, (PeproTech, 200-34), 10 ng/mL GM-CSF, 2 mM Glutamax

Table S4. Antibodies.

	Supplier	Cat No.	WB	IF
IBA1	Abcam	ab5076		1:200
LAMP-1	Cell Signaling Technology	D2D11		1:200
LRRK2 N-Term (N138/6)	NeuroMAB	75-188	1:1000	
LRRK2 C-Term (N241A/34)	NeuroMAB	75-253	1:1000	1:1000
LRRK2 phospho S935	Abcam	ab133450	1:500	
MAP2	Abcam	ab32454		1:1000
pan-14-3-3	Thermo Fisher	51-0700		1:100
RAB5	Cell Signaling Technology	C8B1		1:200
RAB7	Cell Signaling Technology	9367		1:200
RAB8a	Cell Signaling Technology	D22D8		1:200
RAB9	Cell Signaling Technology	5118		1:200
RAB10	Cell Signaling Technology	D36C4		1:200
RAB10	Abcam	ab181367		1:200
pT73 RAB10	Abcam	ab230261		1:200
pT73 RAB10	Abcam	ab241060		1:200
α -Tubulin	Sigma	T5168	1:5000	
IRDye 680RD Goat anti-Rabbit IgG	Li-Cor	926-68071	1:10,000	
IRDye 800CW Goat anti-Mouse IgG	Li-Cor	926-32210	1:10,000	
Donkey anti-mouse Alexa 647	Life Technologies	A31571		1:500
Donkey anti-rabbit Alexa 568	Life Technologies	A10042		1:500

Supplemental Experimental Procedures

Gene editing of hiPSC

A double nickase strategy was employed to generate homozygous *LRRK2* KO hiPSC lines. First, gRNAs (Table S2) were cloned into Cas9 nickase plasmid with puromycin selection (PX462; Addgene, #48141). hiPSCs were transfected by neon-transfection system (Life Technologies) and were seeded in single cell onto 10 cm² tissue-culture treated dish (Fisher) at low density to ensure selection of each individual colony. To screen possible KO clones, genomic DNA was extracted and concentration measured using picogreen (Life Technologies). PCR amplicons were produced by Phusion Hot start DNA polymerase (NEB) on PT-200 PCR machine (MJ Research) and quantitative reverse transcript polymerase chain reaction (qRT-PCR) was carried out with LC Green Plus+ (BioChem) and AmpliTaq master mix (Applied Biosystems) on StepOne plus (Applied Biosystems). Continuous melting step was allowed to screen for aberrant melt curve by using High Resolution Melting Software (Applied Biosystems), and the presence of out-of-frame deletion/insertion was confirmed by sequencing analysis. Similarly, for the repair of heterozygous *LRRK2* G2019S mutation, a donor template was designed with silent mutations in the PAM site to maximize the efficiency of gene-editing and *PstI* site for screening clones.

Western blot

Cells were washed with ice-cold PBS and then lysed directly by adding lysis buffer (50 mM Tris-HCl, 150 mM NaCl, 0.5 mM EDTA, 1 tablet of protease inhibitor (Roche), 100 μ L of phosphatase inhibitor, 1 % maltoside) to a final concentration of 1×10^5 cells/ μ L. Cell lysates were centrifuged at 17,000 rpm for 20 min at 4°C. Pellets were discarded and supernatants were mixed with 4x NuPAGE LDS (lithium dodecyl sulphate) sample buffer and 10x NuPAGE sample reducing agent and were heated for 10 min at 70°C. Each sample containing 25 – 30 μ g of protein was loaded into either 3-8% Tris-Acetate or 4-12% Bis-Tris NuPAGE pre-cast gels. Electrophoresis was performed for 60 min at 120 V using NuPAGE SDS running buffer. Proteins were transferred onto polyvinylidene difluoride (PVDF) membrane using Pierce Power blotter system (Thermo Scientific). iBind Flex system (Life Technologies) was used to blot membranes with antibodies, using iBind Fluorescent Detection (FD) solution kit according to the manufacturer's instructions. The membrane was scanned with Odyssey Sa Infrared Imaging System (Li-Cor) and fluorescence intensity quantified using MyImage analysis software (Thermo Scientific). See Table S3 for antibodies used.

Immunoprecipitation

For crosslinking antibodies to beads, Protein G Sepharose beads (Sigma, P3296) were washed with PBS and incubated with antibody against LRRK2 (NeuroMAB; N241A/34 or N138/6) overnight at 4°C on a rotating wheel. For each preparation of beads, 40 μ g of antibodies and 60 μ L of Protein G Sepharose beads were mixed in 1 mL PBS. Any unbound antibodies were washed off with 1 mL of 0.2 M sodium borate buffer (pH 9.0). Crosslinking was carried out by incubating antibody-bead complexes with 20 mM dimethyl pimelimidate dihydrochloride (DMP; Sigma, D8388) in 0.2 M sodium borate buffer (pH 9.0) for 40 min at RT. Antibody-bead complexes were washed once with 0.2 M ethanolamine (pH 8.0) and were incubated in 0.2 M ethanolamine buffer for 2 h at RT. Beads were quenched with 0.58% v/v acetic acid and 150 mM NaCl. Crosslinked beads were washed three times with PBS and stored in 4°C until used.

Nonspecific proteins were first cleared by incubating whole cell lysates with naked G Sepharose beads on a rotating wheel in 4°C for 30 min. About 20×10^6 to 30×10^6 cells were incubated in 30 μ L of G sepharose beads. Pre-cleared cell lysates were then incubated with G Sepharose beads cross-linked with LRRK2 antibody (NeuroMAB) overnight on a rotating wheel at 4°C. Unbound proteins were washed off three times using lysis buffer without detergents. Finally, LRRK2 interactors were eluted by boiling protein-bead complexes at 70°C for 10 min in SDS elution buffer. See Supplemental information for Mass Spectrometry methodology.

Immunostaining

Cells were fixed with 4% Paraformaldehyde in PBS in RT for 10 min and were blocked and permeabilized overnight at 4°C in blocking buffer containing 5% BSA (Sigma, A7906) and 10% normal donkey serum (Sigma, D9663) and 0.1% Triton-X in PBS. Primary antibody was diluted in blocking buffer and cells were stained for 1 h in RT. See Table S3 for antibodies used.

Unbound antibodies were washed in PBS with 0.3% Triton-X three times, 15 min each. Secondary antibodies (Life Technologies) were diluted 1:500 in blocking buffer containing 0.05% Triton-X and incubated for 1 h at RT. Unbound antibodies were again washed in PBS with 0.3% Triton-X for 15 min, three times. Finally, cells were stained with DAPI in PBS with 0.3% Triton-X for 10 min, and washed three times with PBS. Confocal images were taken by Olympus Fluoview FV1200 (Olympus) or an Opera Phenix High-Content Screening System (PerkinElmer).

Quantification of LRRK2(+) phagosomes using Columbus Image Data Storage and Analysis System

Analysis of confocal images acquired by OperaPhenix (PerkinElmer) began with “Input image” command, which processed z-stack images by stacking with maximum projection. “Find Nuclei” Method B identified the population of nuclei in DAPI channel. “Find Surrounding Region” using Alexa 647 channel defined approximate cell boundaries, ensuring that only internalised zymosan bioparticles are quantified. “Find Spots” identified zymosan bioparticles using Alexa 488 Channel, with a size range defined. “Find Surrounding Region” found regional spots surrounding each identified zymosan bioparticle. “Calculate Intensity Properties” command calculated intensity of LRRK2 signal (Alexa 647 channel) surrounding zymosan bioparticles. “Select Population” quantified the number of LRRK2(+) phagosomes and also the number of LRRK2 super-coated phagosomes by setting thresholds of signal intensity. The same workflow was used to quantify the number of LRRK2(+) phagosomes that displayed positivity for RAB5, 7, 8a, 9, 10 and LAMP-1 (collectively referred to as markers). But in this case, “Calculate Intensity Properties” command was used twice, first to measure the intensity of LRRK2 signal (Alexa 647) and then for the intensity of the marker signal (Alexa 568) within the LRRK2(+) population (or in whole population for the LRRK2-/- experiments).

Real-time phagocytosis assay using pHrodo-labelled zymosan bioparticles

Quantification of acidified phagosomes was evaluated using pHrodo Green zymosan bioparticles (Thermo, P35365). Bioparticles were resuspended in live imaging solution (Thermo, A14291DJ) according to manufacturer's instruction and were sonicated for 10 min (Bioruptor) prior to each experiment. During the assay, 70,000 hiPSC-macrophages in each well of a 96-well clear bottom black plate (Corning, CLS3603) were kept in live imaging solution along with 0.2 mg/mL pHrodo bioparticles. The number of fluorescent bioparticles were monitored every 10 min in InCucyte Live Cell Analysis System (Essen Bioscience) for 2 h. To account for any cell number variability, cells were stained NUCLEAR-ID® Red DNA stain (Enzo Life Sciences) at the end of the phagocytosis experiment. For each acquired image, the total number of fluorescent particles was normalized to the total cell number.

Mass Spectrometry

Samples were trypsin digested and desalted using X18 tips. Samples were analysed on an Ultimate 3000 RSLCnano HPLC (Dionex) system run in direct injection mode coupled to a QExactive Orbitrap mass spectrometer (Thermo Electron). Samples were resolved on a 25cm x 75µm inner diameter picotip analytical column (New Objective) which was packed in-house with ProntoSIL 120-3 C18 Ace-EPS phase, 3µ bead (Bischoff Chromatography). The system was operated at a flow-rate of 300nL min⁻¹. A 120 min gradient was used to separate the peptides. The mass spectrometer was operated in a “Top 10” data dependent acquisition mode. Precursor scans were performed in the orbitrap at a resolving power of 70,000, from which the ten most intense precursor ions were selected by the quadrupole and fragmented by HCD at normalised collision energy of 28%. The quadrupole isolation window was set at 3 m/z. Charge state +1 ions and undetermined charge state ions were rejected from selection for fragmentation. Dynamic exclusion was enabled for 40s. Data were converted from .RAW to .MGF using ProteoWizard (Chambers et al., 2012). Data was collected and analysed on the Central Proteomics Facilities Pipeline (CPFP)(Trudgian et al., 2010).

Supplemental References

- Chambers, M. C., Maclean, B., Burke, R., Amodei, D., Ruderman, D. L., Neumann, S., . . . Mallick, P. (2012). A cross-platform toolkit for mass spectrometry and proteomics. *Nat Biotechnol*, 30(10), 918-920. doi:10.1038/nbt.2377
- Trudgian, D. C., Thomas, B., McGowan, S. J., Kessler, B. M., Salek, M., & Acuto, O. (2010). CPFP: a central proteomics facilities pipeline. *Bioinformatics*, 26(8), 1131-1132. doi:10.1093/bioinformatics/btq081